Formation of the giant Maoping Mississippi Valley-type Pb–Zn (Ge) deposit via fluid mixing: Evidence from trace element and sulfur isotope geochemistry of pyrite

Niu Pp, Jiang Sy, Manuel Munoz

Ore Geology Reviews 169 (2024) 106110

Contents lists available at ScienceDirect

Ore Geology Reviews

journal homepage: www.elsevier.com/locate/oregeorev

Formation of the giant Maoping Mississippi Valley-type Pb–Zn (Ge) deposit via fluid mixing: Evidence from trace element and sulfur isotope geochemistry of pyrite

Pan–Pan Niu [a,b], Shao–Yong Jiang [a,b,*], Manuel Muñoz [c]

[a] Key Laboratory of Geological Survey and Evaluation of Ministry of Education, China University of Geosciences, Wuhan 430074, PR China
[b] State Key Laboratory of Geological Processes and Mineral Resources, Collaborative Innovation Center for Exploration of Strategic Mineral Resources, School of Earth Resources, China University of Geosciences, Wuhan 430074, PR China
[c] Geosciences Montpellier, CNRS UMR 5243, Université de Montpellier, Montpellier 34095, France

ARTICLE INFO

Keywords:
Pyrite
Elemental composition
Sulfur isotope
Maoping Pb–Zn deposit
MVT deposit

ABSTRACT

The SYG (Sichuan–Yunnan–Guizhou) area is one of the most economically significant Mississippi Valley Type (MVT) ore provinces, providing approximately 27 % of the Pb–Zn resources in China. The Pb-Zn deposits in this region are renowned for their high grade, and the Maoping deposit with 20.3 % Pb-Zn grade is one prime example. However, the mechanism of such high-grade mineralization remains unclear, and pyrite may record valuable ore-forming information before and during Pb-Zn mineralization. Based on field geology and petrography, three hydrothermal stages were identified in the Maoping deposit: dolomite–pyrite vein (stage I), dolomite–sphalerite–galena vein (stage II), and calcite vein (stage III). Three types of pyrite are recognized: Py1 and Py2 occur in stage I, and Py3 is closely associated with sphalerite and galena in stage II. Py1 exhibits the highest concentrations of S, Pb, Sb, Cu, Co, Ni, V, Ag, Mn, Se, and Mo, and Py3 shows the highest Fe and As contents but the lowest levels of S, Pb, Sb, Cr, Ti, Co, Ni, Mn, and Mo. The element composition of Py2 shows transitional characteristics between those of Py1 and Py3. The Co and Ni contents gradually decrease from Py1 through Py2 to Py3, while their ratios remain within the range of 0.1–1.0. Compared with Py1 and Py2, Py3 exhibits suddenly elevated As levels and apparent acicular structures, indicating that a rapidly precipitating environment was likely triggered by an abrupt temperature decrease. Py1 exhibits $\delta^{34}S$ values of 19.7–21.5 ‰, followed by Py2 between 18.6 and 21.1 ‰; both indicate that the sulfur was sourced from sulfates by thermochemical sulfate reduction (TSR). In contrast, Py3 exhibits lower $\delta^{34}S$ values ranging from 7.5 to 11.0 ‰, potentially attributed to bacterial sulfate reduction (BSR). The differences in mineral structure, element composition, and sulfur isotopes among the three pyrite types indicate the involvement of two distinct fluids: metal-bearing basin brine and fluid containing reduced sulfur. The former was derived from basin brine that extracted ore metals (Pb^{2+} and Zn^{2+}) from host sedimentary piles. The latter originated from carbonate strata in the Maoping area containing reduced sulfur formed by BSR. We propose that the ore-bearing basin brine reacted with organic matter in the wallrock through TSR to generate Py1 and Py2 in stage I and then mixed with the positioned fluid containing reduced sulfur via BSR to precipitate Py3, sphalerite, and galena in stage II. Hence, fluid mixing is the primary ore-forming mechanism and effectively accounts for the high-grade Pb–Zn ores in the Maoping deposit.

1. Introduction

The presence of pyrite, a highly abundant metal sulfide in Earth's crustal rocks, offers valuable insights into ancient geological phenomena and features such as tectonic movements, global atmospheric oxygenation and reduction processes, as well as volcanic activity and magmatic–hydrothermal systems (e.g., Reddy and Hough, 2013; Large et al., 2014; Large et al., 2019; Mukherjee and Large, 2020; Steadman et al., 2021). Pyrite serves as a primary paragenetic mineral in numerous hydrothermal ore deposits, providing significant insight into fluid conditions and mineralization processes through abundant trace element signatures (Large et al., 2007; Deditius et al., 2011; Genna and Gaboury,

* Corresponding author.
E-mail address: shyjiang@cug.edu.cn (S. Jiang).

https://doi.org/10.1016/j.oregeorev.2024.106110
Received 21 February 2024; Received in revised form 30 April 2024; Accepted 4 June 2024
Available online 7 June 2024

2015; Chinnasamy et al., 2021). Many studies have focused on pyrite from various sediment–hosted gold deposits, orogenic deposits and Carlin–style deposits, due to its role as the uppermost gold–bearing mineral (e.g., Large et al., 2009, 2011; Thomas et al., 2011; Makoundi et al., 2014; Agangi et al., 2015; Jiang et al., 2023). Furthermore, pyrite is commonly studied in Pb–Zn deposits (SEDEX and MVT). For instance, (1) trace elements are utilized to ascertain the origin and composition of ore-forming fluids, as well as the genesis of ores (Gadd et al., 2016; Wang et al., 2018; Song et al., 2019), and (2) sulfur isotopes are employed to trace the source of ore-forming materials and speculate on the ore-forming mechanism (Li et al., 2019a; Zhang et al., 2022). Consequently, despite not being an ore mineral, pyrite still allows for the elucidation of the ore-forming process in Pb–Zn deposits.

The Maoping deposit is one of the largest Pb–Zn deposits within the SYG area, and abundant pyrite types are associated with Pb-Zn mineralization. Several important conclusions regarding the Maoping Pb–Zn deposit have been widely acknowledged: (1) it was deposited during the Late Triassic through Rb–Sr and Sm–Nd isotope dating (Yang et al., 2019 and references therein); (2) its ore-forming materials originated from a combination of underlying basement rocks and overlying marine carbonate rocks (Tan et al., 2019; Xiang et al., 2020); (3) the reduction of marine sulfate supplied reduced sulfur for Pb–Zn mineralization (Kong et al., 2018; Wu et al., 2021); and (4) germanium is mostly found in the sphalerite crystal lattice (Belissont et al., 2016; Cugerone et al., 2020; Chen et al., 2021). However, several issues still require resolution, including (1) the mineralization mechanism—the sulfate reduction or fluid mixing model (Yang et al., 2019; Xiang et al., 2020; Wu et al., 2021), (2) the source of reduced sulfur for Pb–Zn mineralization—TSR or BSR (Tan et al., 2019), and (3) the origin for high-grade ore deposition (averaging 20.3 %, higher than most MVT deposits worldwide: 3–10 %; Leach et al., 2010). The extensive research on trace elements and isotopes in sphalerite and galena cannot accurately reflect pre-ore information, thereby constraining the ore-forming mechanism in the Maoping deposit (Xiang et al., 2020; Wu et al., 2021; Xu et al., 2020). Hence, we conducted comprehensive in situ analyses of element compositions and sulfur isotopes for different pyrite types within the Maoping Pb–Zn deposit to further explore the intricate ore-forming processes responsible for high Pb–Zn grades. Given that the Maoping deposit serves as a typical example, the findings in this study can be extrapolated and applied to Pb–Zn deposits across the entire SYG area.

2. Regional geology

The Yangtze Block is regarded as one of the most ancient cratons in China and was involved in the Paleoproterozoic Columbia and Neoproterozoic Rodinia supercontinents (Fig. 1A; Zheng et al., 2013; Cawood et al., 2013, 2018). The Yangtze Block comprises an Archean to early Neoproterozoic metamorphic basement, which is overlain by sedimentary cover and surrounded by numerous magmatic intrusions from the Neoproterozoic to the Mesozoic (Fig. 1B; Zhang and Zheng, 2013; Zhang et al., 2020; Tang et al., 2021). The northern Yangtze Block is predominantly underlain by the Archean crystalline basement (e.g., Kongling and Douling complex), while the western margin is primarily characterized by the Meso– to Neoproterozoic folded basement (e.g., Kunyang and Huili Formations; Li et al., 2019b; Li et al., 2019c; Xiang et al., 2020). Abundant Neoproterozoic granites and mafic −ultramafic rocks are found in the western and northern parts of the Yangtze Block, respectively (Fig. 1B; Kong et al., 2018; Zhao et al., 2018). During the Mesozoic epoch (Triassic), a large mantle plume triggered the eruption of massive Emeishan basalts, which host world-class Fe–Ti–V oxide deposits (Song et al., 2018; He et al., 2020). Moreover, the Yangtze Block is covered by thick layers of marine and continental sedimentary rocks (Hu et al., 2017; Yang et al., 2019).

The SYG area (the study area), is located at the triangular junction of Sichuan, Yunnan, and Guizhou provinces on the Yangtze Block. This area is bounded by the N-S-trending Anning Fault to the west, the N-S-trending Mile–Shizong Fault to the southeast, and the N-W-trending Weining–Shuicheng Fault to the northwest (Fig. 1B; Han et al., 2019; Xiang et al., 2020). This region generally comprises two basement units, two sedimentary covers, and interbedded Emeishan basalts (He et al., 2020; Wu et al., 2021). The lower basement consists of Archean hypometamorphic crystalline rocks, specifically diorite–granitic schists and gneisses of the Kangding Formation (Zhu et al., 2020; Luo et al., 2022). The upper basement includes the Kunyang and Huili Formations, which are characterized by interstratified slates, shales, carbonates, and volcanic rocks (Wu et al., 2021; Niu et al., 2023). The basement above is overlain by an extensive layered marine sediment sequence formed during the Ediacaran–Permian period, followed by a continental sedimentary unit during the Triassic to Cretaceous (Wu et al., 2013; Xu et al., 2020).

The tectonic framework of the SYG area is characterized by fifteen major faults trending in the N-S, N-E, and N-W directions (Fig. 1B). The N-S-trending faults include the Anninghe–(Lvyejiang) Fault and the Xiaojiang Fault, which underwent initial extensional deformation in a S-W direction, followed by subsequent compression and torsion in the N-S direction (Fig. 1B; Han et al., 2019; Niu et al., 2024). The Anninghe–(Lvyejiang) Fault delineates the separation between Pb–Zn deposits to the east and Fe–Cu–REE deposits associated with intrusions to the west (Fig. 1B; Zhou et al., 2014; Xiang et al., 2020). The Xiaojiang Fault and its subsidiary structures control numerous Pb–Zn deposits, such as Lehong, Daliangzi, and Paoma (Fig. 1B; Yuan et al., 2018; Chen et al., 2019). The N-E-trending fault system dominates the Mile–Shizong Fault, exhibiting several minor secondary faults on its northwestern side. The Weining–Shuicheng Fault is a prominent N-E-trending structure in the SYG area, intersecting with the Mile–Shizong Fault in the southeastern region and extending continually toward the northwest (Fig. 1B; Zhou et al., 2013; Kong et al., 2018).

The magmatic rocks in this region include Neoproterozoic mafic–ultramafic rocks and granitoids, as well as Ordovician–Devonian mafic–ultramafic rocks and the Emeishan basalts (Zhang et al., 2015; Chen et al., 2021; Kong et al., 2018; Fu et al., 2021). Abundant geochronological research has indicated that the formation of the Emeishan basalts (~260 Ma) preceded the Pb–Zn mineralization event (228–191 Ma) in the SYG area (Zhou et al., 2013; Zhang et al., 2015; Yang et al., 2019).

The SYG area is the dominant region in China for Pb–Zn resource production and MVT ore concentration. Currently, there are more than 500 Pb–Zn deposits (occurrences) and approximately 30 Mt Pb–Zn metals hosted in this area, including the Huize, Daliangzi, Maoping, Tianbaoshan, and Maozu deposits (Fig. 1B; Hu et al., 2017; Tan et al., 2019; Chen et al., 2021). Most of these Pb–Zn deposits are found within the marine carbonate sequence from the Neoproterozoic Ediacaran to Permian periods (Kong et al., 2018; Han et al., 2019). Each deposit primarily occurs at a single or multiple stratigraphic positions. For instance, the Huize deposit is located within the Baizuo Formation, while the Maoping deposit is situated within the Zaige and Weining Formations (Chen et al., 2021; Niu et al., 2024). Faults and stratigraphic horizons serve as key controlling factors for Pb–Zn deposits in the SYG area.

3. Deposit geology

The Maoping Pb–Zn deposit hosts 2.5 Mt of metals, with average grades of 14.2 % Zn and 6.1 % Pb. It also contains 560 t of Ag with an average grade of 74.91 g/t and 182 t of Ge with an average grade of 24.00 g/t. The deposit is divided by the NS-trending Luoze River and consists of eastern and western ore clusters, encompassing 37 mined orebodies (Fig. 1C; Zhao et al., 2023; Wu et al., 2024). The eastern part comprises the Nos. I, II, and III ore blocks, which are crucial components and account for more than 80 % of the total resources, while the western part includes the Shuilu, Qiancengdong, and Hongjianshan ore blocks (Fig. 1D; Chen et al., 2021; Niu et al., 2023).

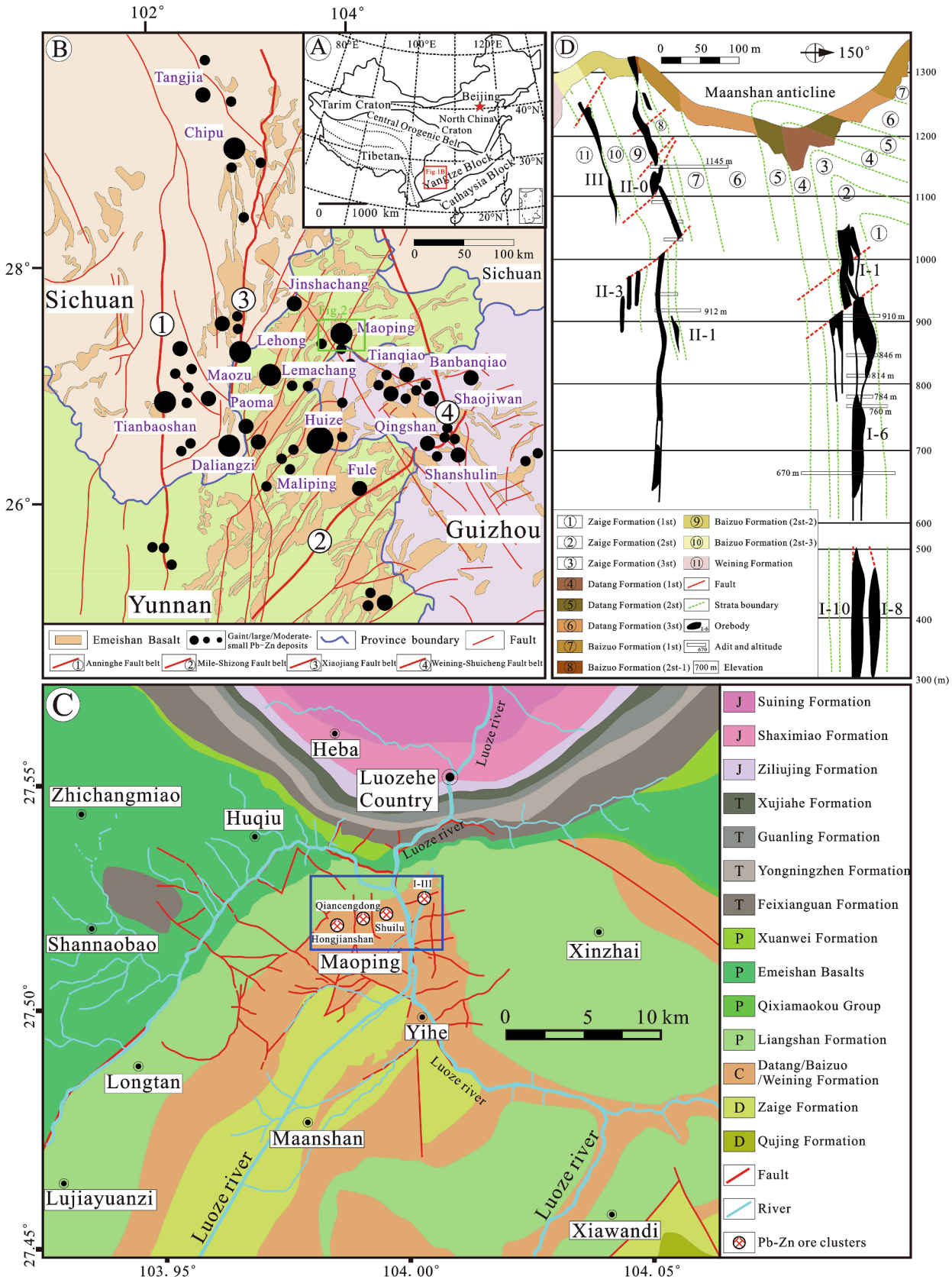

Fig. 1. (A) The main tectonic framework of China, showing the position of the SYG area (after Zhang et al., 2015). (B) Regional geological schematic diagram of the SYG (Sichuan, Yunnan, and Guizhou provinces) clamping area, showing the overlying Emeishan basalts and regional dynamic tectonic conditions (Kong et al., 2018). (C) Geologic diagram of the Maoping Pb–Zn deposit, which displays Pb–Zn ore clusters named I–III, Shuilu, Qiancengdong, and Hongjianshan. (D) Comprehensive vertical profile drawing of the I–III ore clusters in the Maoping Pb–Zn deposit, which include the No. I, I–6, I–8, I–10, II–1, II–3, and III Pb–Zn orebodies (Han et al., 2019).

The exposed strata include the Devonian Zaige Formation, the Carboniferous Datang, Baizuo and Weining Formations, the Permian Liangshan and Qixia–Maokou Formations, the Emeishan basalts, and Quaternary sediments (Fig. 1C). The Zaige Formation is composed of off–white thick coarse-grained dolomite (>120 m), and can be categorized into three sections based on different interbedded marker layers (Chen et al., 2021; Zhao et al., 2023). The No. 1 section comprises dolomite interbedded with thin layers of carbonaceous shale, and the No. 2 section contains algae-bearing dolomite accompanied by a limited amount of shales, carbonaceous shales, and crystalline limestones (Han et al., 2019; Xiang et al., 2020). The No. 3 section is composed of coarse-grained dolomites interspersed with stratified carbonaceous shales (Fig. 1D; Wu et al., 2021; Wang et al., 2023). The Datang Formation is characterized by gray-green and black carbonaceous shale and sandstone, which contain numerous industrial smokeless coal seams (He et al., 2020; Niu et al., 2023). The Baizuo Formation comprises thick-layered and fine-grained gray limestone interbedded with thin-layered calcareous shale and black shale, as well as flint strips and lumps (Fig. 1D; Xiang et al., 2020; Miao et al., 2023). From bottom to top, the lithologies of the Weining Formation include dolomite intercalated with shale and bioclastic limestone, interstratified dolomite and limestone, limestone with shale and dolomite, interbedded dolomite and limestone, and dolomite with flint strips and lumps (Wu et al., 2021; Wang et al., 2023). The Liangshan Formation is composed of sandy shale, tuff, and breccia, with approximately 5 m of bituminous coal on its roof (Tan et al., 2019; Yang et al., 2019). The Qixia–Maokou Formation consists of fine-grained limestones with organic matter, compact limestones, and minor biological fossils (Fig. 1C). The Emeishan basalts and the overlying Quaternary sediments represent younger strata than the Qixia–Maokou Formation (Niu et al., 2023; Wang et al., 2023). The more recent Triassic and Jurassic strata predominantly outcrop in a circular arc distribution in the northern part of this deposit. These strata include the Xuanwei, Feixianguan, Guanling, Xujiahe, Ziliujing, Shaximiao, and Suining Formations, which are characterized by fluvial–lacustrine sedimentary rocks (Fig. 1C).

The Maanshan anticline (below) and the Zhao–Lu anticline (top) constitute the primary structural framework in the Maoping deposit, with the former being the dominant ore-controlling structure (Fig. 1C; Han et al., 2019; Zhao et al., 2023). The Maanshan anticline is a short axial plunging fold with dimensions of 20 km in length and 19 km in width (Fig. 1C). It exhibits a sigmoidal axis ranging from 10° to 37°, an inclination of the southeast wing between 30° and 40°, and an inclination of the northwest wing from 65° to 90° (Fig. 1C; Han et al., 2019). The formation of the Maanshan anticline predates Pb-Zn mineralization (Wu et al., 2021; Zhao et al., 2023). The lithological variations within the Maanshan anticline gradually transition from the Zaige, Datang, Baizuo, and Weining to the Liangshan Formation toward its periphery (Fig. 1C). A series of N-S-, N-E-, and N-W-trending faults situated in the core play essential roles in controlling the Pb–Zn mineralization. The Emeishan basalts situated to the north are primary magmatic rocks near the Maoping deposit and consist of compact massive basalts, as well as almond-shaped and stomatal basalts (Yang et al., 2019; Wu et al., 2024).

The Nos. I, II, and III ore clusters constitute the principal components of the Maoping Pb–Zn deposit. These Pb-Zn orebodies are hosted within the interbedded fault zone in the hinge zone of the Maanshan anticline and exhibit various forms, such as lenticular, layered, veined, and reticulated structures (Fig. 1D). These Pb–Zn orebodies resemble nearly vertical strata that dip toward the southwest (Fig. 1D).

The No. I ore cluster comprises numerous sub-orebodies, such as Nos. I–1, I–6, I–7, I–8, and I–10, hosted by the 2nd section of the Devonian Zaige Formation. The No. I–1 orebody is connected to the deep-seated No. I–6 orebody, which both constitute the largest orebody in this deposit between 620 and 1040 m (Fig. 1D). The Nos. I–8 and I–10 orebodies exhibit similarities between 300–500 m elevations and exhibit barrel and layer shapes (Fig. 1D). The No. II ore cluster is composed of the Nos. II–0, II–1, and II–3 orebodies with Pb–Zn grades of 1.2–30.3 %, locally exceeding 40 % (Han et al., 2019). These orebodies are predominantly found in the dolomite and limestone of the Carboniferous Baizuo Formation. The No. III ore cluster comprises a series of small orebodies that are hosted in the Carboniferous Weining Formation and arranged like a string of beads along fractures (Fig. 1D). In the eastern part of the Maoping Pb–Zn deposit, the Shuilu and Qiancengdong ore clusters exhibit relatively more minor scales than the economically significant Hongjianshan ore cluster, which benefits from the recent discovery of several large Pb-Zn orebodies (Zhao et al., 2023; Niu et al., 2023). Overall, these orebodies in Maoping exhibit substantial vertical extension, expanding as occurrence slows down and contracting rapidly as occurrence changes steeply (Fig. 1D). The ore grades increase gradually from top to bottom, accompanied by a decrease in Zn content but an increase in Pb content (Han et al., 2019).

The ore-forming process of the Maoping Pb–Zn deposit can be divided into three periods: the sedimentary diagenesis period, hydrothermal period, and supergene period (Fig. 2). In the early passive continental margin environment, the Maoping area was deposited by a series of thick-layered marine carbonates consisting of abundant dolomite and limestone, minor pyrite and bitumen, and trace barite. The hydrothermal period comprises three stages: dolomite-pyrite veins in stage I, dolomite-sphalerite-galena veins in stage II, and calcite veins in stage III (Fig. 3A, B). The dominant minerals in stage I include dolomite and pyrite, with less sphalerite, galena, and calcite (Fig. 3C). Stage II is characterized by abundant sphalerite and galena, with localized dolomite, calcite, pyrite, bitumen, quartz, and boulangerite (Fig. 3D). There are also rare miargyrite and zinckenite grains in stage II. Only abundant (Fe–) calcites are prominently visible, and other minerals are scarce in stage III (Fig. 3E). The supergene period is dominated by oxidized minerals, such as hematite, siderite, limonite, and smithsonite, which were likely oxidized from pyrite, sphalerite, and galena (Fig. 2).

4. Sampling and petrography

The collected samples are from the Nos. I–6, I–7, and I–8 orebodies within the No. I ore cluster and the No. H-8 orebody in the Hongjianshan ore cluster, as well as some drillings and surface mineralization. Three types of pyrite are observed before and during Pb–Zn mineralization, namely, coarse-grained pyrite (Py1) and fine-grained pyrite (Py2) in stage I, and middle-graiedn pyrite (Py3) in stage II. The Py1 aggregations exhibit compact lumps and megaphyric structures, wherein the pyrite particles demonstrate superior quality and are relatively closely packed (Fig. 4A; Fig. 5A, B). Py2 is commonly found and is often associated with dolomite as the primary mineral assemblage in stage I (Fig. 4B). Compared with Py1, Py2 shows excellent grain sizes and brecciated structures, and the bonds between grains are looser, with many voids and fissures (Fig. 5C, D). Under natural light, Py3 appears to be a highly conspicuous bright yellow color. It is interspersed with Py1 and Py2 and is closely related to galena-sphalerite veins (Fig. 4C-E). Although Py3 predates sphalerite and galena, they exhibit a very close relationship (Fig. 5E, F). In other words, the emergence of Py3 is invariably accompanied by sphalerite and galena in all the samples. Py1 is distributed within Py2 as compact and massive structures, while Py3 is interspersed with Py1 (Fig. 5G-J). Py3, sphalerite, and galena veins are distributed in the interior of Py2 (Fig. 5E, F, H, I). Two distinct structures can be observed in Py3: granular and acicular. The acicular structure of Py3 becomes particularly prominent when it coexists with sphalerite and galena (Fig. 5E, H, I). The calcite in stage III is interspersed with and replaces minerals formed during stages I and II (Fig. 4F; Fig. 5J, L).

5. Analytical methods

5.1. Electron probe micro–analysis (EPMA)

Electron probe micro-analysis of pyrite was conducted at the State Key Laboratory of Geological Processes and Mineral Resources, China

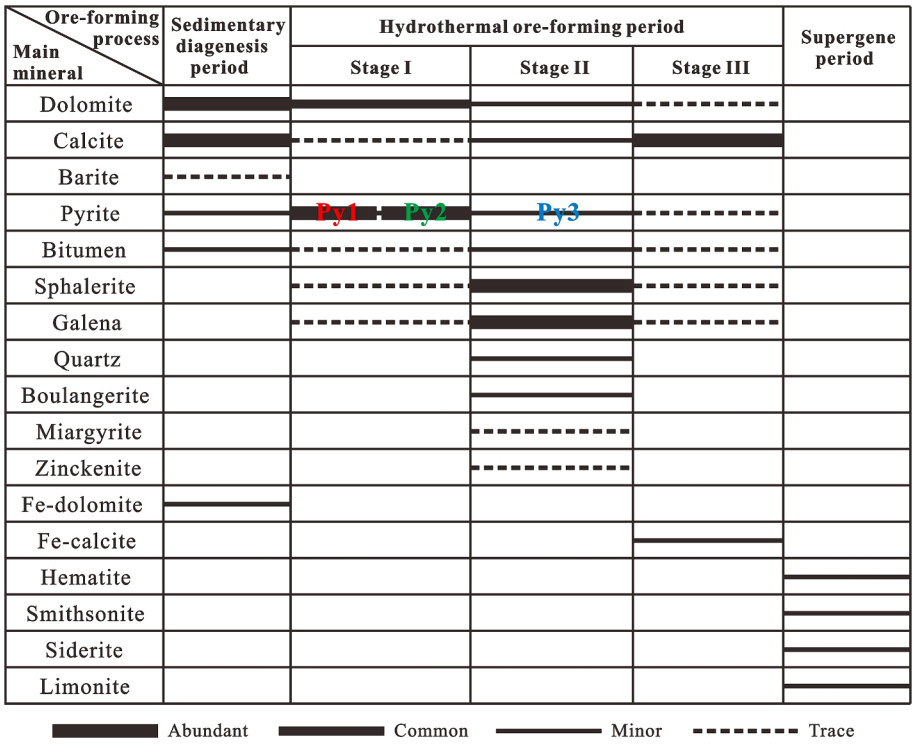

Fig. 2. Relative period diagram of the mineral sequence and paragenetic association of the Maoping Pb–Zn deposit. Abbreviations: Py1– "coarse-grained pyrite", Py2– "fine-grained pyrite", Py3– "medium-grained pyrite".

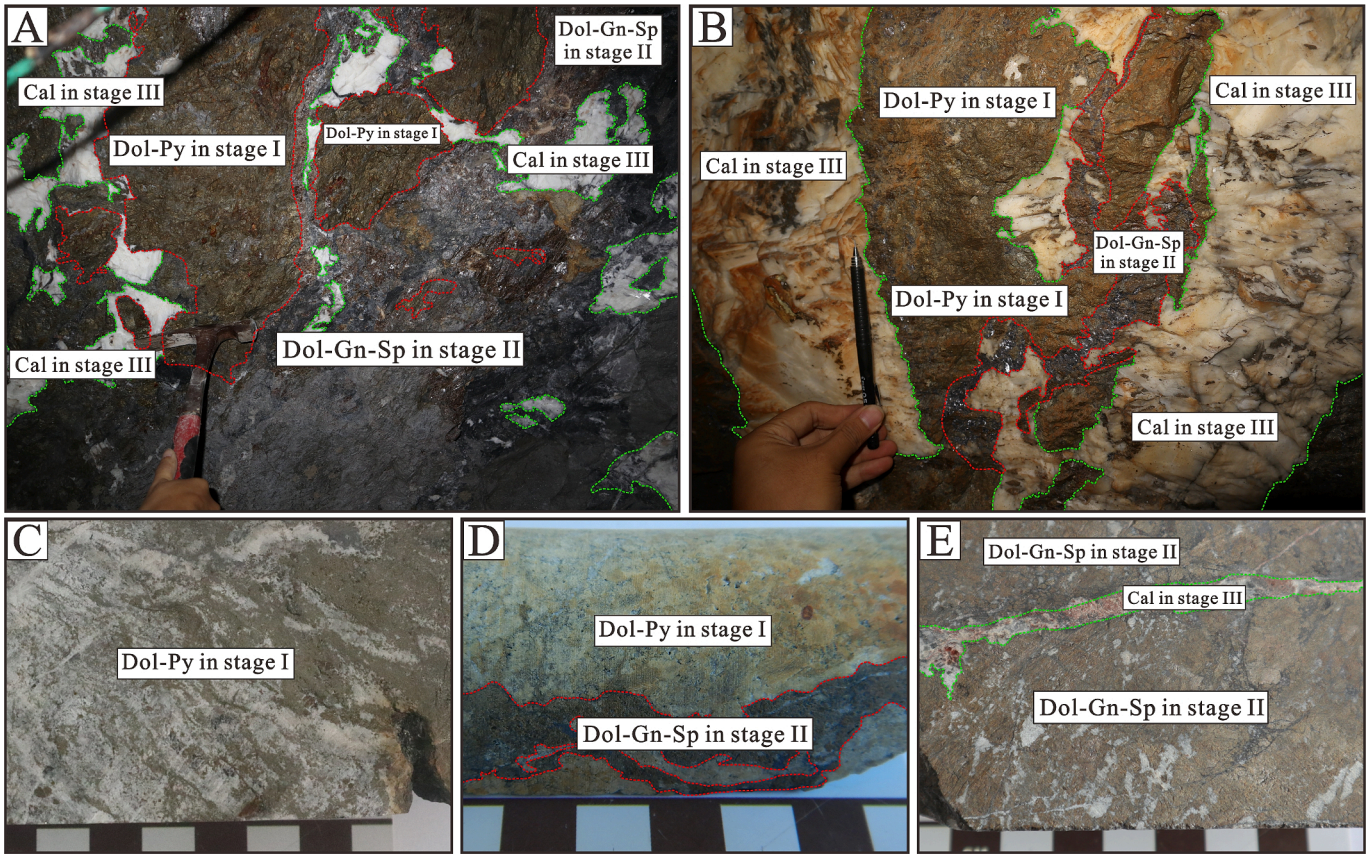

Fig. 3. (A, B) Photographs of Pb–Zn mineralization inside the underground trench, showing three hydrothermal stages of the hydrothermal ore–forming period: (1) stage I: Dol–Py veins, (2) stage II: Dol–Gn–Sp veins, and (3) stage III: Cal veins; (C) the Dol–Py vein in stage I; (D) the Dol–Py veins in stage I interspersed by the Dol–Gn–Sp veins in stage II; (E) the Cal veins in stage III cross-cutting the Dol–Gn–Sp veins in stage II. Abbreviations: Dol– "dolomite", Py– "pyrite", Gn– "galena", Sp– "sphalerite", Cal– "calcite".

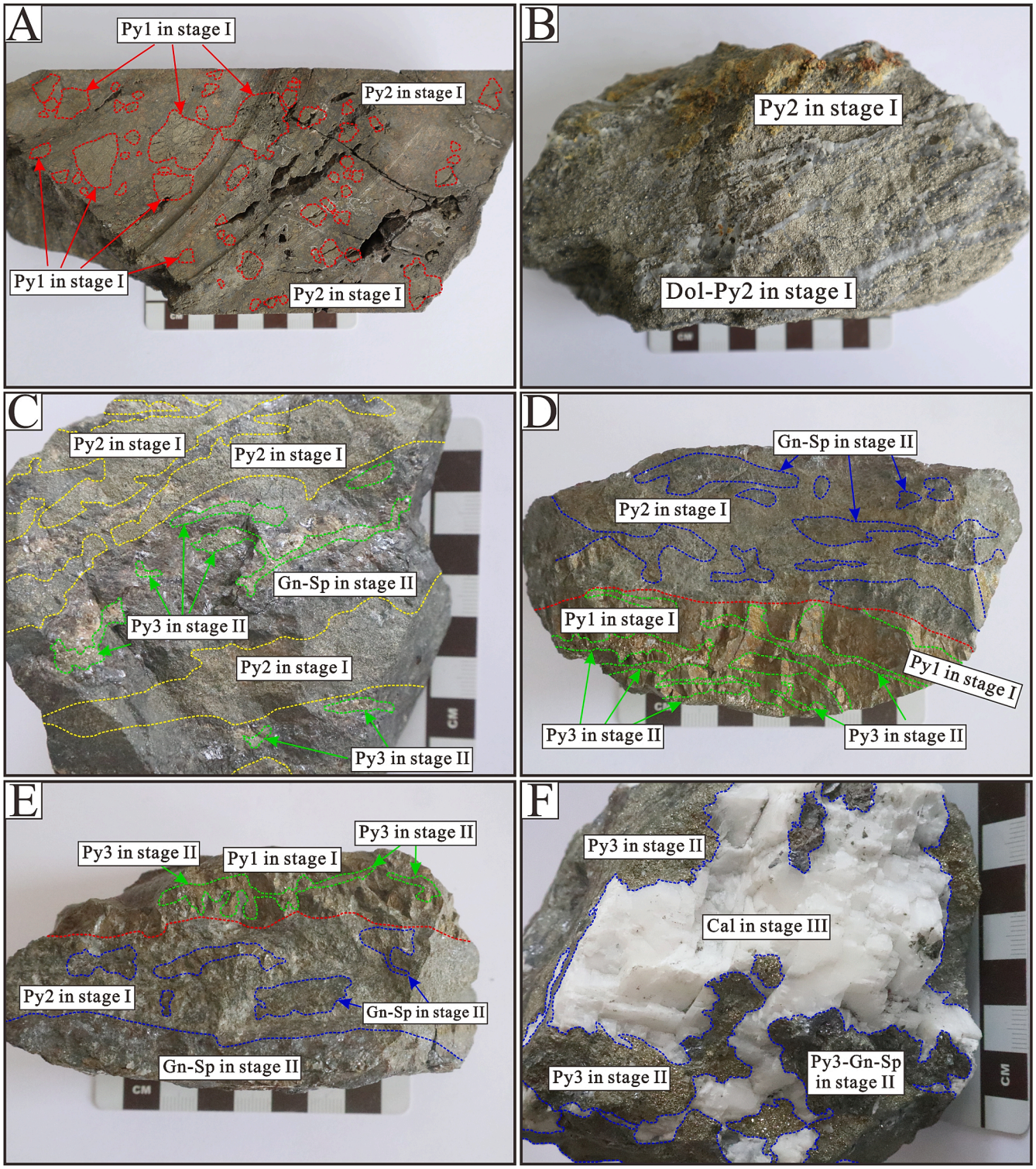

Fig. 4. Hand specimen photographs selected from the Maoping Pb–Zn deposit. (A) Py2 parceling Py1 at stage I; (B) Dol–Py2 veins in stage I galena-sphalerite-dolomite veins with medium-grained pyrite in stage II cross-cutting fine-grained pyrite in stage I; (C) Py3, Gn, and Sp in stage II cross-cutting Py2 veins in stage I; (D–E) Py1 and Py2 in stage I interspersed with Py3, Gn, and Sp veins in stage II; (F) Cal veins in stage III in the holes and crevices of Py2–Gn–Sp veins in stage II. Abbreviations: Dol– "dolomite", Py– "pyrite", Gn– "galena", Sp– "sphalerite", Cal– "calcite".

University of Geosciences (Wuhan). The analysis was performed using a JEOL JXA–8100 model EPM Analyzer connected to a four-channel WDS. Before the formal analysis, the surface of the selected probe sheet was cleaned and then coated with a uniform thickness of carbon (~20 nm) using a carbon spraying instrument (Zhang and Yang, 2016). During the analysis, the EPM Analyzer was operated with analytical parameters, including an acceleration voltage of 15 kV, a current of 20nA, and an electron beam spot diameter of 2 μm. The upper and lower background measurement times were half of the peak measurement time. The elements analyzed in this study included Fe, S, As, Cu, Pb, and Sb, and their corresponding master standards were pyrite, gallium arsenide, cuprite, galena, and elemental antimony, respectively. All the data were

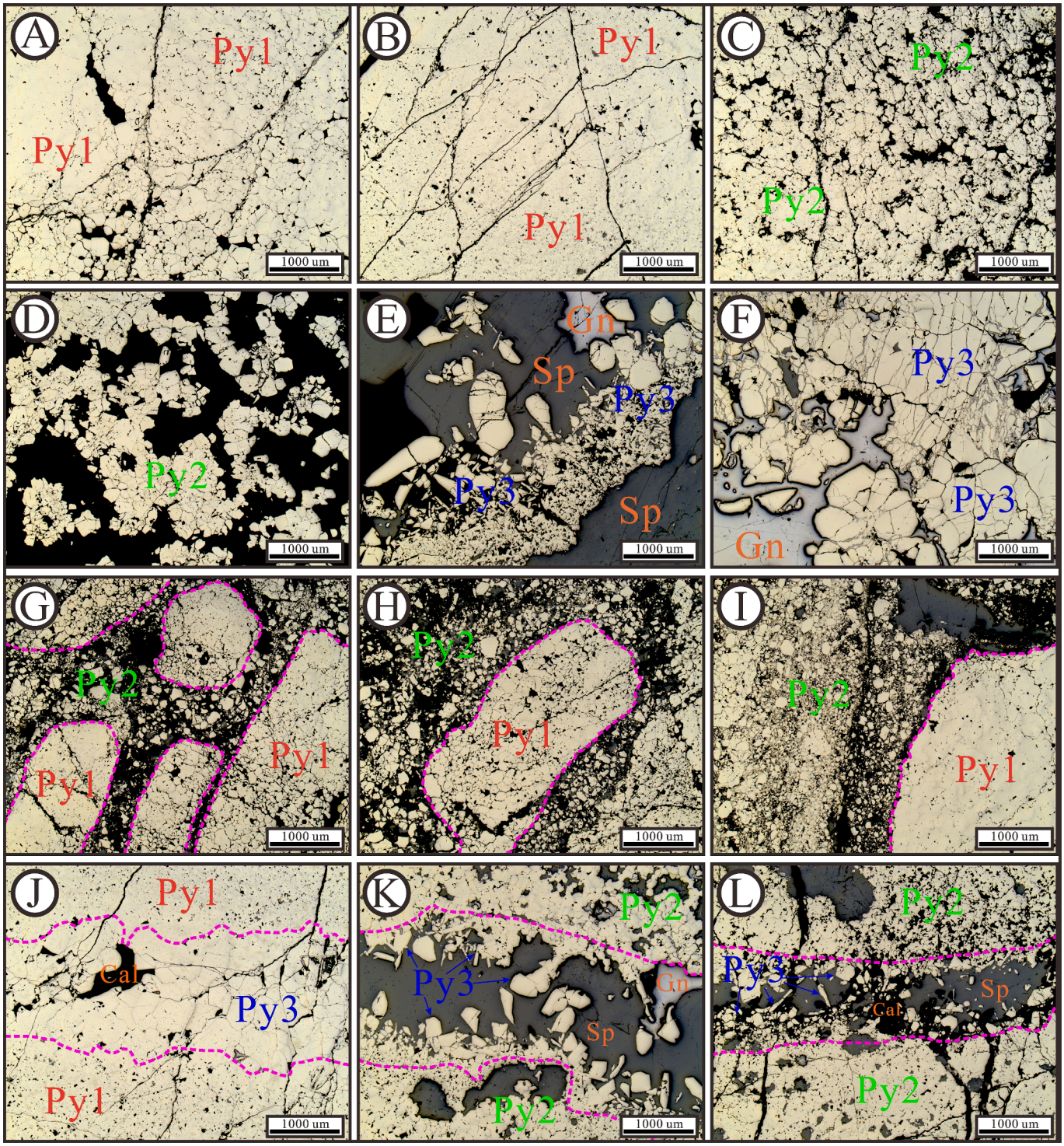

Fig. 5. Photomicrographs of three types of pyrites in the Maoping Pb–Zn deposit. (A, B) Py1 in stage I with massive grain sizes and fewer interparticle cracks; (C, D) Py2 in stage I with large pores between mineral aggregates; (E, F) Py3 in stage II coexisting with Gn and Sp; (G–I) Py2 encapsulating Py1 in stage I; (J) Py1 in stage I interspersed with Py3 in stage II; (K, L) Py3 in stage II, together with galena and sphalerite, crosscutting Py2 in stage I. Abbreviations: Dol– "dolomite", Py– "pyrite", Gn– "galena", Sp– "sphalerite", Cal– "calcite".

corrected online via the ZAF method before generating the output report.

5.2. *Laser ablation inductively coupled plasma-mass spectrometry (LA–ICP–MS)*

The elemental mapping analysis of pyrite was conducted at Nanjing FocuMS Technology Co., Ltd., using a 7900 model quadrupole ICP–MS manufactured by Agilent Technologies, which was connected to a 193 nm ArF laser ablation system. The mapping analysis was performed through continuous line scanning, with each line scanning distance matching the size of the beam spot. The laser ablation process employed a beam spot of 40 μm and an energy level of 2–3 J/cm^2 at a frequency of 10 Hz. The step size in the line scanning process is consistent with the

size of the beam spot. The He gas was the carrier gas during the laser ablation process, while Ar gas acted as an auxiliary gas to adjust the sensitivity. Standard samples were measured before and after the entire ablation process, and background signal values were collected for 30 s. Given our larger analyzed area, the mapping analysis process was successfully completed within one hour to ensure data accuracy. The raw data were processed by LIMS software to output elemental mapping, in which the instrument signal drift correction and background deduction were completed automatically (Xiao et al., 2018).

The elemental content analysis of pyrite at specific points was conducted at Nanjing FocuMS Technology Co., Ltd., utilizing an Agilent 7700x quadrupole ICP–MS and an Analyte Excite laser ablation system. The laser generated a homogenized deep ultraviolet beam, which was applied to the pyrite surface for 40 s, with an energy density of 6.06 J/cm^2, a beam diameter of 40 μm, and a frequency of 6 Hz. Prior to analysis, each analyzed position underwent pre-ablation to eliminate impurities and oxides from the surface. The denuded samples were subsequently mixed with He gas and Ar gas before being subjected to ICP–MS analysis. This study used two internal standards (MASS–1 and GSE–1G). The raw data were processed using the ICPMSDataCal software through a 100 % normalization strategy without incorporating internal standards (Liu et al., 2008). The elements analyzed included Na, Mg, Al, Si, S, K, Ca, Sc, Ti, V, Cr, Mn, Fe, Co, Ni, Cu, Zn, Ga, Ge, As, Se, Rb, Sr, Y, Mo, Ag, Cd, In, Sn, Sb, Te, Ba, W, Au, Tl, Bi, Pb, Th and U. The trace element data of pyrite in this paper were corrected using the Fe content as determined by EPMA data.

5.3. Multi–collector inductively coupled plasma-mass spectrometry (MC–ICP–MS)

The in situ sulfur isotope analysis of pyrite was performed at the Mineral Deposit Geochemistry Division of the State Key Laboratory of Geological Processes and Mineral Resources, China University of Geosciences (Wuhan). This analysis employed a Nu Plasma II MC–ICP–MS and a Resonetics–S155 laser ablation system. The laser emitted a homogenized 193 nm deep ultraviolet beam onto the mineral surface, with a spot diameter of 23 μm. This process was conducted at a frequency of 5 Hz and 40 s for every position. The denuded sample was mixed with high–purity He gas and trace amounts of Ar and N gases, to generate an aerosol within the mass spectrometer. The $^{34}S/^{32}S$ ratio of the selected sample was directly obtained, and the $\delta^{34}S$ ratio was subsequently calculated using the standard–sample bracket method based on laboratory pyrite standard samples of WS–1 and WS–2 (Zhu et al., 2017). The detailed analysis methods can be found in Niu et al. (2019), and the overall analytical precision (1σ) is approximately ± 0.1 ‰.

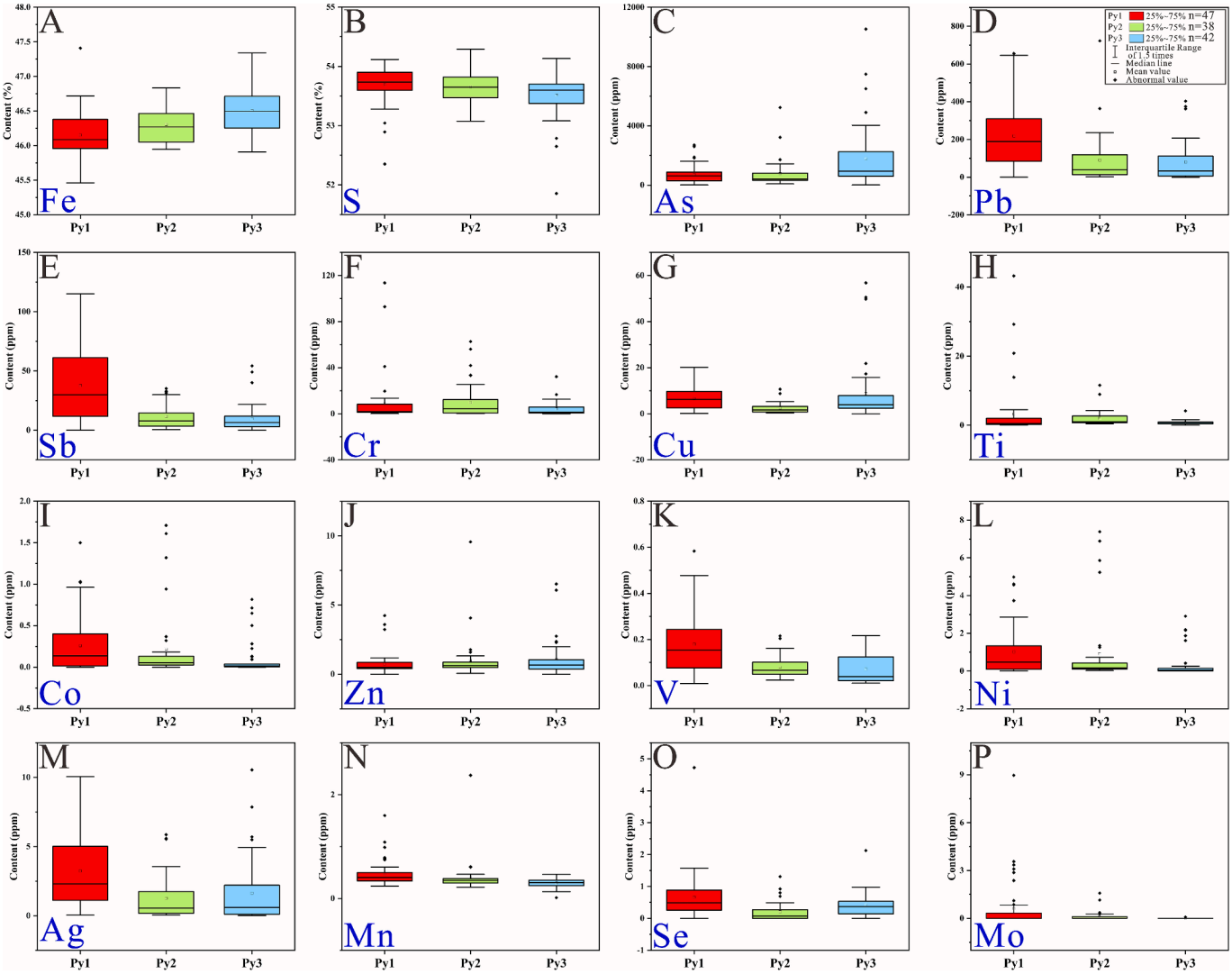

Fig. 6. Elemental boxplots of Py1, Py2, and Py3 analyzed by LA–ICP–MS; the elements included Fe, S, As, Pb, Sb, Cr, Cu, Ti, Co, Zn, V, Ni, Ag, Mn, Se, and Mo (A–P). Abbreviations: Py1– "coarse-grained pyrite", Py2– "fine-grained pyrite", Py3– "medium-grained pyrite".

6. Results

6.1. EPMA data for pyrite

A total of 127 data points from three types of pyrite (Py1, Py2, and Py3) are reported in Table S1 and include Fe, S, Cu, Pb, As, and Sb contents. Py1 contains 45.46–47.41 % Fe, 52.35–54.12 % S, 0–1.70 % As, 0–0.60 % Pb, 0–0.20 % Cu, and 0–0.02 % Sb, with total concentrations ranging from 99.52 to 100.66 %. The dominant elements in Py2 are Fe (45.95–46.83 %) and S (53.01–54.29 %), accompanied by minor elements such as As (0–0.56 %), Cu (0–0.02 %), Pb (0–0.09 %) and Sb (0–0.04 %). These elements contribute to a total content between 99.56 and 100.72 % (Fig. 6A, B). The composition of Py3 includes Fe, S, As, Cu, Pb, and Sb, with varying contents ranging from 45.91–47.34 %, 51.86–54.13 %, 0–2.16 %, 0–0.04 %, 0–0.10 %, and 0–0.02 % respectively, resulting in total values ranging from 99.67–100.76 % (Table S1).

6.2. Pyrite element mapping analysis

We selected two representative pyrite areas for elemental mapping analysis. The first mapping (21MP–11–1) involves the intersection of Py3 with Py1, covering an area of approximately 0.32 cm^2. This particular area exhibits minor instances of sphalerite, galena, and calcite in the fillings (Fig. 7A). The Fe and S signals show no significant variation throughout the region, except for lower levels of Fe and S in areas where calcite, galena, and sphalerite are present (Fig. 7B, C). Py1 shows more pronounced Ag signals than Py3, and galena contains the highest amount of Ag (Fig. 7D). The As, Mg, and Zn signals of Py1 and Py3 are slightly low, while the elevated signals observed in certain areas can be attributed to the influence of sphalerite and calcite (Fig. 7E–G). The signals of Co, Cu, Sb, Tl, V, and Ni in Py3 are lower than those in Py1; however, most of these elements exhibit high signal values within calcite (e.g., Co, Cu, V, and Ni; Fig. 7 H–M).

The second sample (21MP–27–1) covers an area of approximately 0.34 cm^2 and consists of Py3, sphalerite, and galena from stage II interspersed with Py2 from stage I (Fig. 8A). The Fe and S signals in Py2 and Py3 are greater than those in sphalerite and galena (Fig. 8A, B). The Ag, Zn, and Sb primarily originate from galena and sphalerite but are relatively depleted in pyrite and sphalerite (Fig. 8D, G, J). Compared to that in Py2, the As signal in Py3 is remarkably strong, especially in the area near sphalerite (Fig. 8E). The Mg, Co, Tl, V, and Ni signal values decrease gradually from Py2 to Py3, while their signals are lost within sphalerite (Fig. 8H, K–M). Cu is locally enriched without obvious patterns in Py1 and Py2 (Fig. 8I).

6.3. Pyrite LA-ICP-MS trace element analysis

The time-integrated signals of each element in the three types of pyrite exhibit relatively smooth profiles with minimal sharp peaks, particularly for Fe, S, Pb, As, and Sb (Fig. 9A–C). These findings confirm

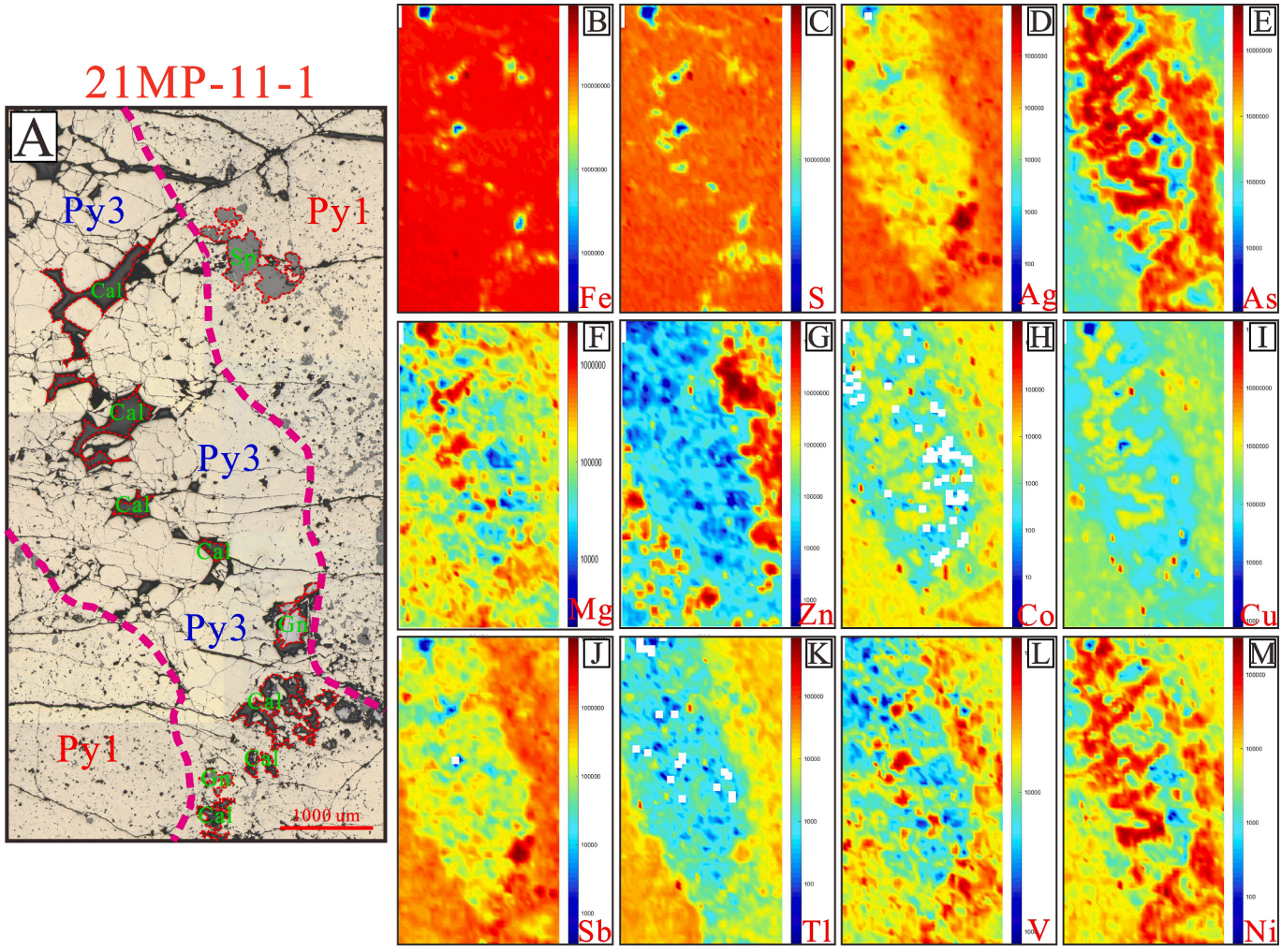

Fig. 7. Representative LA–ICP–MS elemental mapping (21MP–11–1) of Py3 cross–cutting Py1, including Fe, S, Ag, As, Mg, Zn, Co, Cu, Sb, Tl, V, and Ni with scales in counts–per–second. Abbreviations: Py– "pyrite", Sp– "sphalerite", Gn– "galena", Cal– "calcite".

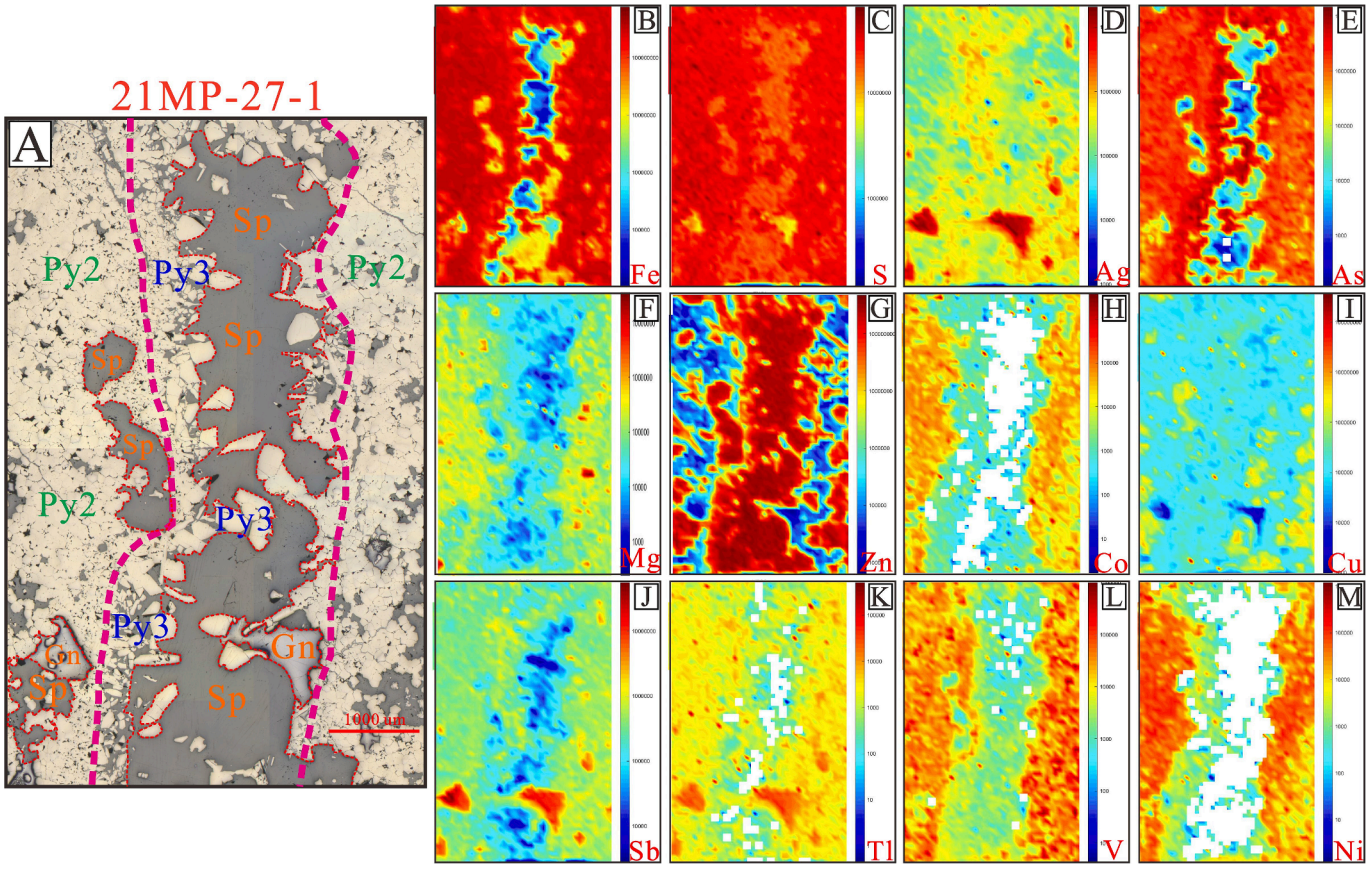

Fig. 8. Representative LA–ICP–MS elemental mapping (21MP–27–1) of Py_2 interspersed with Py_3 LA–ICP–MS, including Fe, S, Ag, As, Mg, Zn, Co, Cu, Sb, Tl, V, and Ni with scales in counts–per–second. Abbreviations: Py– "pyrite", Sp– "sphalerite", Gn– "galena".

that these elements are not present as microscale mineral inclusions but rather exist as evenly distributed nanoscale inclusions or as element substitutions in the pyrite lattice (Atienza et al., 2023; Fougerouse et al., 2023; Niu et al., 2024). LA-ICP-MS could not detect nanoscale inclusions; thus, it was also categorized as an element substitution in this study. Only a few data reveal the presence of microscale mineral inclusions such as galena (Pb), sphalerite (Zn), dolomite (Mg, Ca), albite (Na, Sr), and K–feldspar (K, Al, Si), which are confirmed by abrupt elemental signal curves (Fig. 9D–H). The data affected by the microscale inclusions did not represent the natural pyrite composition and were consequently excluded from this study. A total of 127 LA–ICP–MS data points corresponding to the EPMA data points are summarized in Table S2.

The As contents of Py1 (7–2701 ppm, mean = 705 ppm) and Py2 (80–5239 ppm, mean = 776 ppm) are significantly lower than the As contents of 8–10534 ppm (mean = 1770 ppm) observed in Py3 (Fig. 6C). The Pb contents in Py2 (1–723 ppm, mean = 90 ppm) and Py3 (0–403 ppm, mean = 80 ppm) are marginally lower than those in Py1 (0–656 ppm, mean = 219 ppm; Fig. 6D). This is consistent with the variation trends observed for Sb concentrations in Py1 (0–115 ppm, mean = 38 ppm), Py2 (1–35 ppm, mean = 12 ppm), and Py3 (0–54 ppm, mean = 10 ppm; Fig. 6D, E). Py1 and Py2 contain higher Cr contents of 0–114 ppm (mean = 9 ppm) and 0–63 ppm (mean = 10 ppm), respectively, than Py3 (0–32 ppm, mean = 4 ppm) (Fig. 6F). Py1 has a Cu content of 1–20 ppm (7 ppm on average), which is lower than that of Py2 (0–11 ppm) but significantly greater than that of Py3 (0–57 ppm) (Fig. 6G). Py1 contains the highest contents of Ti (0–43 ppm), Co (0–2 ppm), V (0–1 ppm), Ni (0–5 ppm), Mn (0–2 ppm), and Mo (0–9 ppm), which gradually decrease from Py2 to Py3 (Fig. 6H, I, K, L, N, P). There is minimal variation in Zn content among Py1 (0–4 ppm), Py2 (0–10 ppm), and Py3 (0–7 ppm) (Fig. 6J). The most significant concentrations of Ag (0–10 ppm) and Se (0–5 ppm) can be observed in Py1, followed by Py2 and Py3 (Fig. 6M, O).

6.4. Principal component analyses of element composition

The log-transformed EPMA and LA–ICP–MS data for the three types of pyrite were subjected to principal component analysis (PCA) using the PCA module of Origin software (Koch, 2012; Frenzel et al., 2016). The contents of S, Mn, Fe, Co, Ni, Cu, Zn, As, Ag, Sb, and Pb were utilized for principal component analysis (PCA). Among the eleven principal components (PC) analyzed, PC1 and PC2 account for 38.9 % and 17.6 %, respectively, representing the distinctive characteristics of the three types of pyrite (Fig. 10A). According to the binary diagram depicting PC1 and PC2, S plays a significant role in the second quadrant while As, Fe, Cu, and Mn contribute significantly in the fourth quadrant. The remaining elements, including Ag, Sb, Pb, Zn, Co, and Ni, are distributed predominantly in the first quadrant (Fig. 10B). The data points corresponding to Py1 and Py2 are primarily clustered along the direction of the second and fourth quadrants. In contrast, the data points associated with Py3 are dispersed mainly along the direction of the first and third quadrants (Fig. 10B). This observation indicates that compared to Py1 and Py2, there is a significant variation in the element composition within Py3, which is primarily influenced by Fe, As, Cu, Mn, Ag, Pb, Sb, and S. Although both Py1 and Py2 exhibit similar elemental characteristics, the differences in Sb, Pb, Ag, Co, and Ni compositions result in distinct confidence ellipse shapes and positions on the PC1 and PC2 binary scatter plots (Fig. 10B).

6.5. Sulfur isotope analysis of pyrite

A total of 105 analyzed spots of in situ S isotopes on three types of

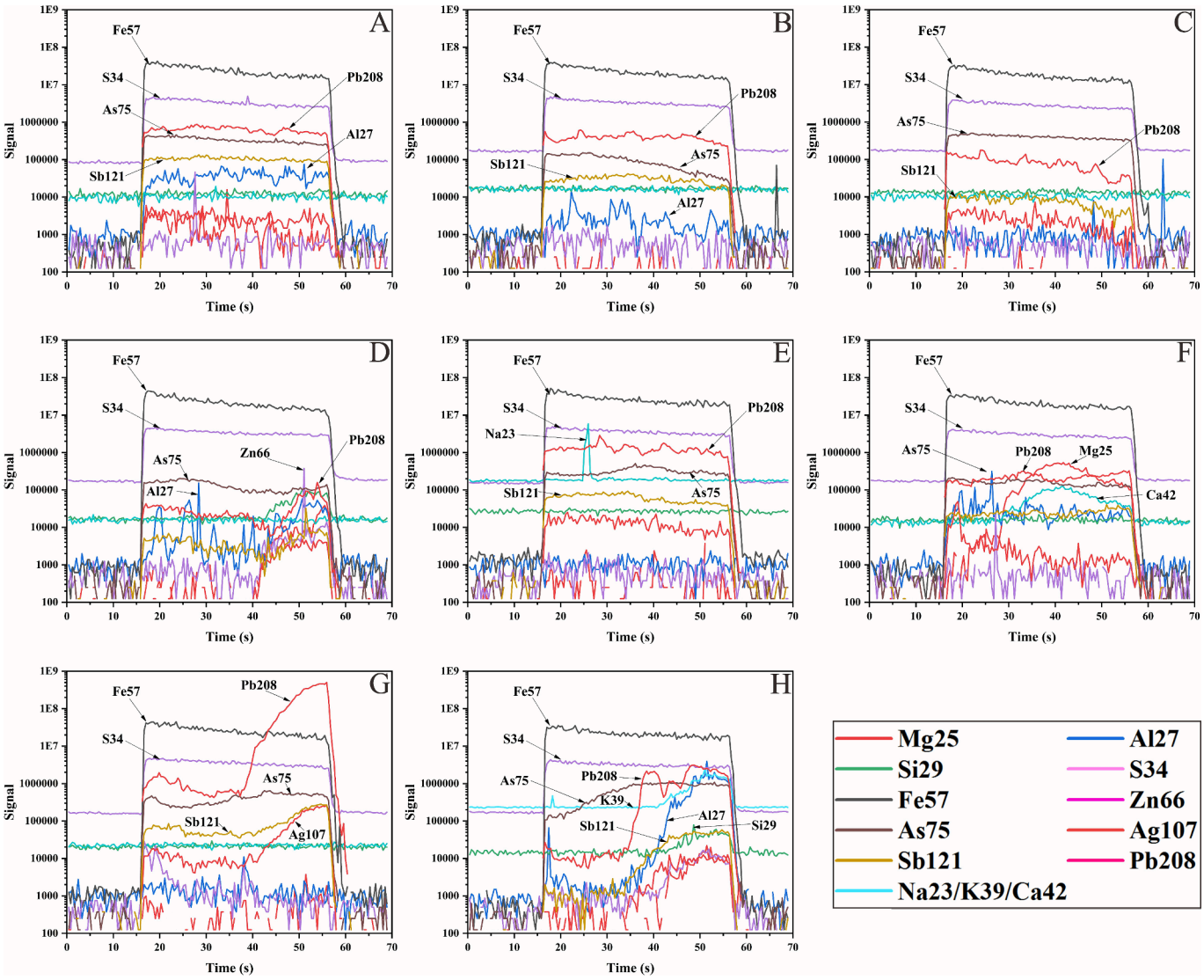

Fig. 9. Elemental time-integrated signals for analyzed spots on typical Py1 (A), Py2 (B), and Py3 (C) with smooth curves, and obtrusive element signals indicating mineral inclusions of galena (D, H), sphalerite (D, E), dolomite (F), albite (G) and K–feldspar (H). Abbreviations: Py1– "coarse-grained pyrite", Py2– "fine-grained pyrite", Py3– "medium-grained pyrite".

pyrite in the Maoping Pb–Zn deposit are illustrated in Fig. 11 and Table S3. The $\delta^{34}S$ values of Py1 range from 19.7–21.5 ‰, with an average of 20.4 ‰ (n = 30), and the $\delta^{34}S$ values of Py2 range from 18.6 to 21.1 ‰, with an average of 19.7 ‰ (n = 30). Py3 has relatively more negative $\delta^{34}S$ values than Py1 and Py2, which are between 7.5 and 11.0 ‰ (mean = 9.4 ‰, n = 45).

7. Discussion

7.1. Trace element variability of pyrite

Pyrite (FeS_2) has a nominal S/Fe atomic ratio of 2:1, with a typical variability of less than 1 % attributed to the incorporation of other trace elements (Chandra and Gerson, 2010; Baya et al., 2021). From Py1 through Py2 to Py3, the Fe content gradually increases, while the S content gradually decreases, resulting in a downward trend in the S/Fe ratio (Fig. 6A, B; Fig. 12A). The As, Pb, Sb, Cu, Co, Ni and Ag contents show significant variations among the three t pyrite types (Fig. 6C–E, G, I, L, M). Numerous trace elements in pyrite can be attributed to solid solutions (element substitution) and micro/nano–inclusions (Deditius and Reich, 2016; Atienza et al., 2023). Compared with Py2 and Py3, Py1 has higher Pb, Sb, Cu, Co, V, Ni, Ag, Mn, Se, and Mo contents (Fig. 6D, E, G, I, K, L, M, O, P). Given that the data affected by microscale inclusions have been excluded, we assume that these elements entered the pyrite lattice through element substitution (Fig. 9A–C). Notably, Py1 exhibits relatively high concentrations of Pb, Sb, and Ag (Fig. 6D, E, M). Due to their large ionic radius, these elements have difficulty entering into the pyrite lattice (Keith et al., 2016; Steadman et al., 2021). The distributions of Pb, Sb, and Ag in the binary diagrams of PC1 and PC2 are also completely independent of S and Fe (Fig. 10B). Hence, we hypothesize that these elements may originate from evenly distributed nanoscale galena inclusions within pyrite (George et al., 2015). Temperature plays an essential role in promoting element substitution in pyrite. Thus, pyrite that forms at high temperatures typically contains more trace elements (e.g., Cu, Co, Ni, Se, Te, and Bi; Craig et al., 1998; Large et al., 2007, 2009; Genna and Gaboury, 2015; Keith et al., 2016). Therefore, Py1 may have formed in a high-temperature environment, and the properties of the ore-bearing fluid during stage I may have been recorded (i.e., significant enrichment of various metal ions). Most of the elemental compositions of Py2 fall within the range between Py1 and Py3, especially those of Fe, S, As, Pb, Sb, Co, Ni, Mn, and Mo (Fig. 6A–E, I, L, N, P). This suggests that Py2 exhibits the transitional characteristics

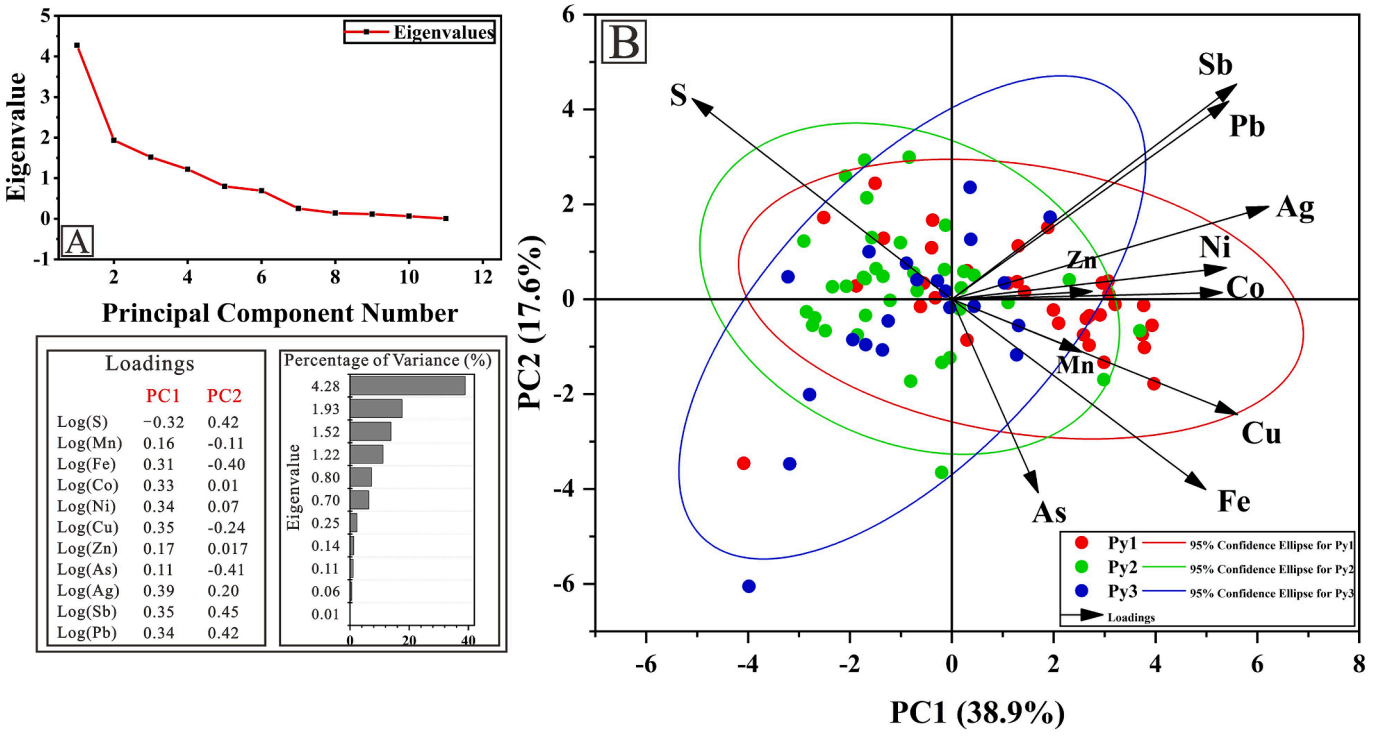

Fig. 10. The principal component analysis results of pyrite element composition, showing the eigenvalues of eleven principal components (A) and the binary scatter plots of PC1 and PC2 (B).

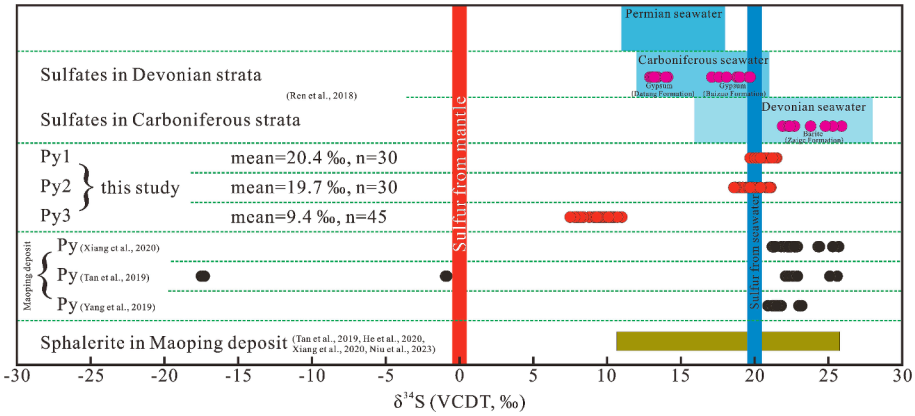

Fig. 11. Scatter diagram of sulfur isotopes of pyrite in the Maoping Pb–Zn deposit, showing the present isotopic data for pyrite and sphalerite in the Maoping deposit, and sulfates and seawater from the Permian, Carboniferous and Devonian, as well as for sulfur from the mantle and seawater (data from Hoefs, 2015; Ren et al., 2018; Tan et al., 2019; Yang et al., 2019; Xiang et al., 2020; He et al., 2020; Niu et al., 2023).

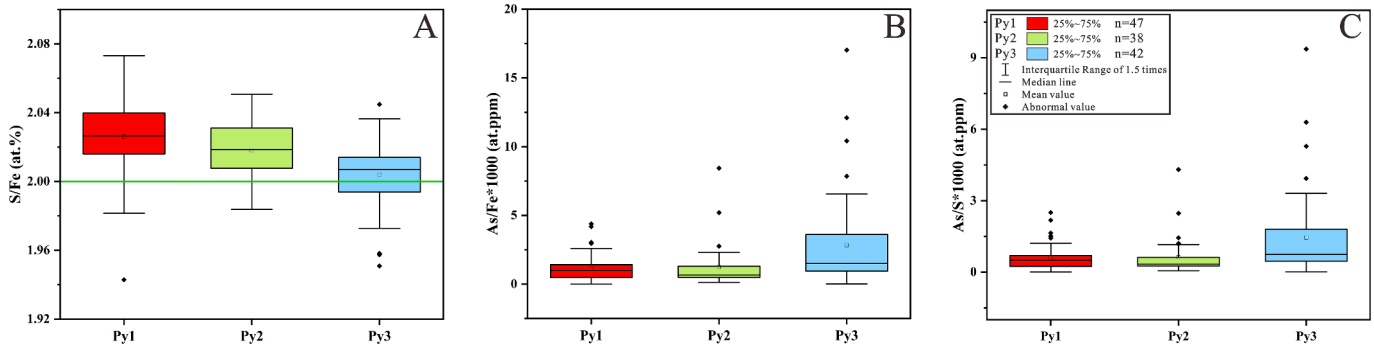

Fig. 12. Elemental boxplots of the atomic ratios of Py1, Py2, and Py3, including (A) S/Fe (at. %), (B) As/Fe*1000 (at. ppm) and (C) As/S*1000 (at. ppm). Abbreviations: Py1– "coarse-grained pyrite", Py2– "fine-grained pyrite", Py3– "medium-grained pyrite".

and formation environment of Py1 and Py3 (e.g., temperature; Large et al., 2011; Hou et al., 2015). Compared with Py3, the elemental composition of Py2 is more similar to that of Py1, but there are certain variations in the contents of Sb, Pb, Ag, Co, and Ni (Fig. 10B).

In comparison to Py1 and Py2, Py3 exhibits a markedly different elemental signature, in particular an abnormally elevated As content (8–10534 ppm), implying physical and chemical mutation conditions in stage II relative to stage I (Fig. 6C; Fig. 12B, C). The predominant form of arsenic in natural hydrothermal fluid is $As(OH)_3$, and the As content in aqueous fluid is influenced by fluid temperature, pH, and H_2S content. At shallow-water hydrothermal systems, lower temperatures, greater alkalinity, lower H_2S contents, and lower As contents are correlated with each other (Breuer and Pichler, 2013; Deditius et al., 2014; Xing et al., 2019; Schrader et al., 2021). Arsenic can be incorporated into pyrite through the following reaction: $FeS_2 + As(OH)_3 \rightarrow FeAsS + H_2S + 1.2O_2 + 0{\cdot}.5H_2O$; thus, low sulfur fugacity and oxygen fugacity favor the introduction of arsenic into pyrite (Pokrovski et al., 2002; Perfetti et al., 2008). High As levels in pyrite suggest a low-temperature environment, as there is a negative correlation between As content and temperature (Deditius et al., 2014; Xing et al., 2019). The presence of Py3 with an unusually high As content suggests a sudden decrease in temperature or sulfur/oxygen fugacity during stage II (Fig. 6C). Pyrite with elevated As content in a metastable mineral assemblage reflects an environment where the mineral precipitates rapidly (Abraitis et al., 2004; Reich and Becker, 2006; Baya et al., 2021). Due to high precipitation rates, minerals typically exhibit a colloidal or acicular structure, which can also be observed in Py3 (Fig. 5E, K, L; Baya et al., 2021; Luo et al., 2022). Therefore, we believe that there was a significant change in fluid properties from stage I to stage II, possibly due to fluid mixing, fluid boiling, or other reasons. Nevertheless, compared with those in Py2, the contents of Cu, V, Ag, and Se in Py3 increase slightly. This could be attributed to an elevated concentration of As, which tends to distort the crystal lattice of pyrite, resulting in defect formation and favoring the incorporation of these trace elements in Py3 (Fig. 6 G, K, M, O; Deditius et al., 2008; Gregory et al., 2015).

High Co and Ni contents in pyrite are thought to correspond to a high–temperature formation environment, as high temperature is beneficial for Co and Ni to form continuous FeS_2–CoS_2 solid solutions and unconnected FeS_2–NiS_2 solid solutions in pyrite (Koglin et al., 2010; Large et al., 2014; Li et al., 2014; Reich et al., 2016). From Py1 through Py2 to Py3, the Co and Ni contents gradually decrease (Fig. 13), as evidenced by the elemental mappings, indicating a gradual decrease in temperature (Fig. 6I, L; Fig. 7F, L; Fig. 8F, L). Therefore, the fluid properties, particularly the temperature, significantly changed from stage I to stage II in the Maoping deposit.

7.2. Origin of sulfur

Seawater sulfate serves as a significant sulfur source in the MVT Pb–Zn deposit, primarily through two main mechanisms, namely TSR and BSR, especially in the SYG area (Leach et al., 2005; Wang et al., 2014; Zhou et al., 2014; Xu et al., 2020). The $\delta^{34}S$ value of sulfide is also influenced by temperature and whether the system is open or closed (Leach et al., 2005). Microthermometry reveals that the fluid inclusions in Maoping sphalerite exhibit complete homogenization temperatures ranging from 200 to 300 °C (Han et al., 2019). In comparison to that in closed systems, sulfate reduction in open systems is faster and results in significantly greater sulfur isotope fractionation (Seal, 2006). TSR requires a high temperature (>150 °C), and a high temperature will accelerate the reaction: $SO_4^{2-} + 2C$ (organic matter) $\rightarrow S^{2-} + 2CO_2$ (Worden et al., 1995; Leach et al., 2005).

Extensive in situ sulfur isotope studies from the Maoping deposit have shown that the $\delta^{34}S$ values of pyrite range between + 20 ‰ and + 27 ‰, which is consistent with the findings for sulfates in ore–host Carboniferous strata (Ren et al., 2018; Yang et al., 2019; Tan et al., 2019; Xiang et al., 2020). Hence, TSR is considered the source of reduced sulfur required for mineralization due to its ability to produce limited sulfur isotope fractionation ($\triangle^{34}S$ (SO_4^{2-}-S^{2-}) < 15 ‰; Xiang et al., 2020). In this study, Py1 in stage I exhibited $\delta^{34}S$ values ranging from 19.7–21.5 ‰, followed by slightly lower $\delta^{34}S$ values between 18.6 and 21.1 ‰ in Py2 in stage I (Fig. 11). Py1and Py2 have similar sulfur isotopic compositions to those of average seawater (20 ‰) and

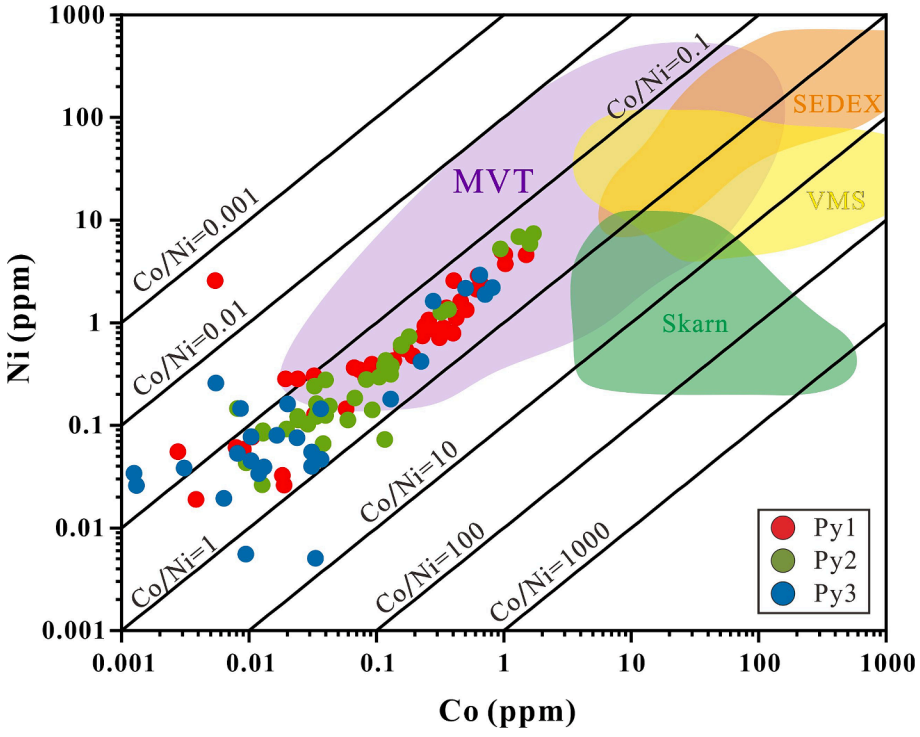

Fig. 13. Binary diagram of the logarithmic coordinates between Co (ppm) and Ni (ppm) in the three types of pyrite in the Maoping Pb–Zn deposit (after Wu et al., 2020).

Carboniferous and Devonian seawater (12.0–21.0 ‰ and 16.0–28.0 ‰, respectively; Fig. 11). Furthermore, the $\delta^{34}S$ values in Py1 and Py2 are close to those of published pyrite and sulfates from the Devonian and Carboniferous strata in the Maoping Pb–Zn deposit (e.g., Yang et al., 2019; Tan et al., 2019; Xiang et al., 2020). Therefore, we believe that the reduced sulfur in Py1 and Py2 can be attributed to the TSR from sulfates in the Carboniferous and Devonian strata (Baizuo and Zaige Formations), thereby aligning with previous research findings. The BSR in the closed system also does not lead to a significant reduction in $\delta^{34}S$ values in sulfides; however, the elevated ore-forming temperature (>200 °C) in the Maoping deposit restricts the presence of BSR (Seal, 2006; Han et al., 2019).

Py3 in stage II, closely related to Pb–Zn mineralization, exhibits a more hostile and scattered sulfur isotopic composition ($\delta^{34}S$ values: 7.5–11.0 ‰; Fig. 11; Table S3). The maximum sulfur isotope fractionation of Py3 is 12.5 ‰, which exceeds that of Py1 and Py2 (no more than 2 ‰), if we assume that sulfate originates from seawater ($\delta^{34}S$ values: 20 ‰; Fig. 11). The sulfur isotope fractionation caused by TSR is clearly influenced by temperature, as increased temperature promotes the transformation from organic reduction to inorganic reduction, resulting in a significant increase in sulfur isotope fractionation (Ohmoto and Rye, 1979). However, from Py1 to Py2 to Py3, the ore-forming fluid exhibited decreasing temperatures, which ruled out apparent sulfur isotope fractionation in Py3 caused by an increase in temperature (Fig. 11; Fig. 13). Therefore, the reduced sulfur in Py3 was not formed by the TSR process. Compared to TSR, BSR could generate more significant fractionation of sulfur isotopes at lower temperatures (up to 40 ‰; Basuki et al., 2008; Shelton et al., 2008; Leach et al., 2010). However, the ore-forming temperature (200 to 300 °C) of the Maoping deposit exceeds the conditions required for BSR (<150 °C), indicating that the reduced sulfur for Py3 formed before Py1 and Py2 rather than during the migration of the ore-bearing basin brine (Bradley and Leach, 2003; Leach et al., 2005). These reduced sulfur compounds in Py3 may have originated from a long-term BSR process within surrounding rocks that were deposited before the arrival of ore-bearing basin brine. Hence, the slight decrease in sulfur isotopic composition from Py1 to Py2 in stage I can be explained by persistent TSR, while Py3 in stage II formed due to the involvement of another source of reduced sulfur through BSR.

7.3. Ore-forming mechanism

Basin brine is widely acknowledged to play a crucial role in the MVT Pb–Zn deposit, as it selectively extracts ore-forming metals (e.g., Pb and Zn) from various geological units and subsequently transports them to favorable positions for precipitation (e.g., Leach et al., 2001, 2005, 2010). However, the ore-forming mechanisms of the Maoping Pb–Zn deposit remain contentious; for example, (1) sulfate reduction mode: the reduced sulfur required for Pb-Zn mineralization was derived from the TSR between sulfate ions in the ore-bearing basin brine and organic matter within the strata, which then combined with metal ions to precipitate (Yang et al., 2019); and (2) fluid mixing mode: the reduced sulfur needed for Pb-Zn mineralization originated from the long-term BSR of sulfate in the strata, and subsequently mixed with the ore-bearing basin brine for precipitation (Xiang et al., 2020; Wu et al., 2021). In this study, decreasing Co and Ni contents from Py1 through Py2 to Py3 indicate gradually decreasing temperatures (Fig. 5I, L; Fig. 13; Reich et al., 2016). The abrupt increase in As content and acicular structure in Py3 represents a sudden change in fluid properties (temperature, pH, and sulfur fugacity), most likely caused by fluid mixing (Fig. 12B, C; Deditius et al., 2014; Xing et al., 2019; Schrader et al., 2021). The sulfur isotopes confirm that the reduced sulfur in Py3 originates from BSR, unlike the TSR in Py1 and Py2 (Fig. 11). The subsequent sphalerite contains $\delta^{34}S$ levels between Py1, Py2 and Py3, indicating the significant contribution of fluid mixing to the mineralization process (Fig. 11; Tan et al., 2019; He et al., 2020; Niu et al., 2024). Therefore, we suggest that the ore-bearing basin brine formed large amounts of pyrite (Py1 and Py2) and minor amounts of galena and sphalerite through TSR with organic matter in the wallrocks (marine carbonate; Fig. 14A, B; Worden et al., 1995; Leach et al., 2005; Zhou et al., 2013). When the ore-bearing basin brine mixed with the positioned fluid containing reduced sulfur through the BSR, the fluid temperature suddenly decreased, and the following reactions occurred: (1) $2S^{-}+Fe^{2+}\rightarrow FeS_2$, (2) $S^{2-}+Zn^{2+}\rightarrow ZnS$, and (3) $S^{2-}+Pb^{2+}\rightarrow PbS$ (Fig. 14C; Zhou et al., 2014; Niu et al., 2019). This process resulted in the precipitation of Py3, galena, and sphalerite in a supersaturated and unbalanced crystalline fluid during stage II (Fig. 4B–D; Fig. 14C; Wilkinson and Eyre, 2005; Bare et al., 2009; Pfaff et al., 2011). The rapid precipitation of sphalerite and galena facilitated a swift reduction in metal ions (Py^{2+}, Pb^{2+}, Zn^{2+}, Ag^{+}) and reduced sulfur (S^{2-}) contents in the fluid, and resulted in the subsequent formation of pure calcite veins in stage III, which were interspersed with and filled in the present mineral assemblage (Fig. 4F; Fig. 14D).

The Maoping deposit has a significantly high average Pb + Zn grade of 20.3 %, with a local grade of > 40 %, which is far greater than most Pb + Zn grades of the MVT deposit throughout the world (3–10 %; Leach et al., 2010). The Pb–Zn orebodies in Maoping exhibit significant vertical extension (>1200 m) along nearly vertical interlayer faults, indicating that the ore–forming fluids were transported through these interbedded faults and effectively mixed with fluids containing reducing sulfur (Fig. 1C, D; Fig. 14). The presence of interbedded faults provided suitable mineralization space for subsequent Pb–Zn mineralization. Consequently, we suggest that the high ore grade of the Maoping Pb–Zn deposit can be attributed to (1) rapid and sufficient fluid mixing, resulting in rapid precipitation of ore-forming materials (Wu et al., 2021; Wang et al., 2023); and (2) the significant presence of steeply interbedded faults, which provided mineralization space and prevented further migration of the ore-bearing basin brine (Zhao et al., 2023).

The Pb–Zn deposits in the SYG area are classified as Huize–type (HZT) MVT deposits, which share similar characteristics: (1) higher average Pb–Zn grade, such as in Huize (24.15 %), Maoping (20.30 %), Qingshan (32.20 %), Lehong (12.03 %), Maliping (15.89 %), Maozu (11.4 %), and Tianbaoshan (10.65 %); (2) fault–controlled distribution of Pb–Zn orebodies; and (3) more significant vertical extension compared to horizontal extension of the Pb–Zn orebody (Han et al., 2019; Leach and Song, 2019). Although the fluid mixing model has been widely accepted for these deposits based on abundant isotope data (e.g., S, Zn, Pb, Zn), the pyrite in this study directly records the Pb–Zn mineralization process caused by fluid mixing (Xiang et al., 2020; Wu et al., 2021; Xu et al., 2020). This study further confirms that the higher grade of Pb–Zn in the deposit within the SYG area can be explained by the fluid mixing model.

8. Conclusions

(1) Three types of pyrite have been identified in the Maoping Pb-Zn deposit, with Py1 and Py2 forming during stage I and Py3 precipitating simultaneously with Pb-Zn mineralization during stage II.
(2) Py1 is characterized by the lowest Fe content but the highest levels of S, Pb, Sb, Cu, Co, Ni, V, Ag, Mn, Se, and Mo. On the other hand, Py3 exhibits the highest Fe and As contents but the lowest levels of S, Pb, Sb, Cr, Ti, Co, Ni, Mn, and Mo. Py2 exhibits a transitional characteristic between Py1 and Py3.
(3) The presence of an acicular structure and high As levels, coupled with low Co and Ni contents, suggest that Py3 formed in a rapidly precipitating environment.
(4) The reduced sulfur in Py1 and Py2 was from thermochemical sulfate reduction (TSR), whereas in Py3, it originated from bacterial sulfate reduction (BSR).
(5) The mixing of metal-bearing basin fluid and fluid containing reduced sulfur is the main mechanism for the mineralization and formation of high-grade ores.

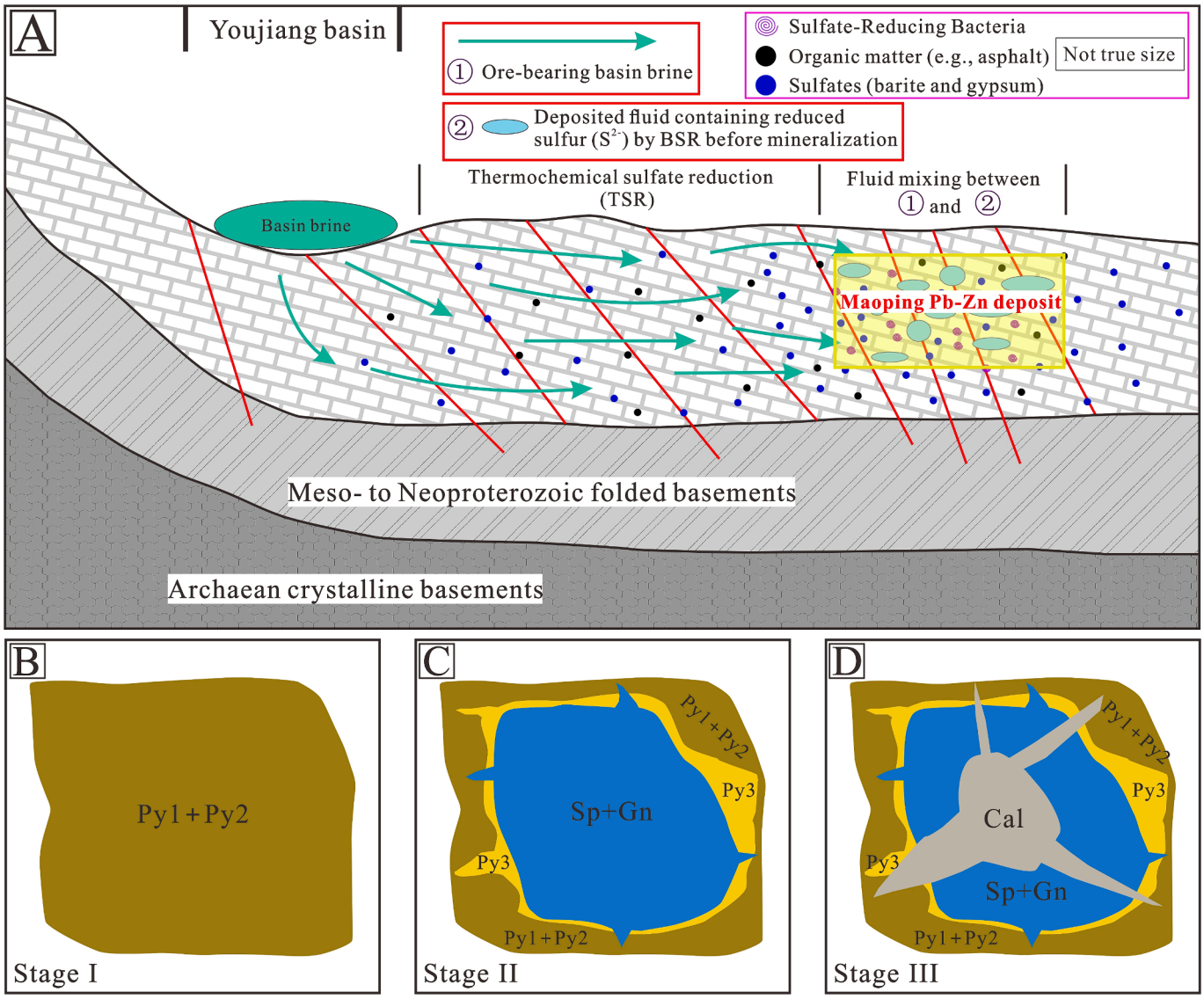

Fig. 14. (A) Genetic model of the Maoping Pb–Zn deposit showing the process of basin brine migration and eventual mixing with fluid containing reduced sulfur to Pb–Zn mineralization; (B–D) Formation model of three pyrite types, namely, sphalerite, galena, and calcite, in the Maoping deposit.

Declaration of competing interest

The authors declare that they have no known competing financial interests or personal relationships that could have appeared to influence the work reported in this paper.

Data availability

All the data are available in the manuscript as Supplementary Tables, and are also available from the corresponding author upon request.

Acknowledgments

We thank Mr. Zhu Peng and Guo Tengda for their help during the course of sample analyses. This study was financially supported by grants from the National Key Research and Development Program of China (2021YFC2900300), the National Natural Science Foundation of China (92162323), and the program of China Scholarships Council (No. 202106410073).

Appendix A. Supplementary data

Supplementary data to this article can be found online at https://doi.org/10.1016/j.oregeorev.2024.106110.

References

Abraitis, P.K., Pattrick, R.A.D., Vaughan, D.J., 2004. Variations in the compositional, textural and electrical properties of natural pyrite: a review. Int. J. Miner. Process. 74, 41–59.

Agangi, A., Hofmann, A., Rollion-Bard, C., Marin-Carbonne, J., Cavalazzi, B., Large, R., Meffre, S., 2015. Gold accumulation in the Archaean Witwatersrand Basin, South Africa—evidence from concentrically laminated pyrite. Earth Sci. Rev. 140, 27–53.

Atienza, N.M.M., Gregory, D.D., Taylor, S.D., Swing, M., Perea, D.E., Owens, J.D., Lyons, T.W., 2023. Refined views of ancient ocean chemistry: tracking trace element incorporation in pyrite framboids using atom probe tomography. Geochim. Cosmochim. Acta 357, 1–12.

Bare, C.D., Boyce, A.J., Boyle, A.P., Williams, P.J., Blake, K., Wilkinson, J.J., Lowther, M., McDermott, P., Prior, D.J., 2009. On the growth of colloform textures: a case study of sphalerite from the Galmoy ore body, Ireland. J. Geol. Soc. London 166, 563–582.

Basuki, N.I., Taylor, B.E., Spooner, E.T.C., 2008. Sulfur isotope evidence for thermochemical reduction of dissolved sulfate in Mississippi Valley type zinc–lead mineralization, Bongara area, northern Peru. Econ. Geol. 103, 183–799.

Baya, C., Le Pape, P., Baptiste, B., Brest, J., Landrot, G., Elkaim, E., Noel, V., Blanchard, M., Ona-Nguema, G., Juillot, F., Morin, G., 2021. Influence of trace level

As or Ni on pyrite formation kinetics at low temperature. Geochim. Cosmochim. Acta 300, 333–353.
Belissont, R., Muñoz, M., Boiron, M.-C., Luais, B., Mathon, O., 2016. Determination of the oxidation state of Ge, Cu and Fe in zoned Ge–rich sphalerite: integrated μ– XRF mappings and μ–XANES study. Geochim. Cosmochim. Acta 177, 298–314.
Bradley, D.C., Leach, D.L., 2003. Tectonic controls of Mississippi Valley-type lead–zinc mineralization in orogenic forelands. Miner. Deposita 38, 652–667.
Breuer, C., Pichler, T., 2013. Arsenic in marine hydrothermal fluids. Chem. Geol. 348, 2–14.
Cawood, P.A., Wang, Y.J., Xu, Y.J., Zhao, G.C., 2013. Locating South China in Rodinia and Gondwana: a fragment of greater India lithosphere? Geology 41, 903–906.
Cawood, P.A., Zhao, G.C., Yao, J.L., Wang, W., Xu, Y.J., Wang, Y.J., 2018. Reconstructing South China in phanerozoic and precambrian supercontinents. Earth Sci. Rev. 186, 173–194.
Chandra, A.P., Gerson, A.R., 2010. The mechanisms of pyrite oxidation and leaching: a fundamental perspective. Surf. Sci. Rep. 65, 293–315.
Chen, W., Ye, L., Hu, Y.S., Danyushevskiy, L., Li, Z.L., Huang, Z.L., 2019. Distribution and occurrence of Ge and related trace elements in sphalerite from the Lehong carbonate-hosted Zn-Pb deposit, northeastern Yunnan, China: insights from SEM and LA-ICP-MS studies. Ore Geol. Rev. 115, 103175.
Chen, W., Ye, L., Hu, Y.S., Huang, Z.L., Danyushevsky, L., Wang, H.Y., 2021. LA–ICP–MS analyses of trace elements in base metal sulfides from carbonate–hosted Zn–Pb deposits, South China: a case study of the Maoping deposit. Ore Geol. Rev. 130, 103945.
Chinnasamy, S.S., Hazarika, P., Pal, D., Sen, R., Govindaraj, G., 2021. Pyrite textures and trace element compositions from the granodiorite–hosted gold deposit at Jonnagiri, eastern Dharwar Craton, India: Implications for gold mineralization processes. Econ. Geol. 116, 559–579.
Craig, J.R., Vokes, F.M., Solberg, T.N., 1998. Pyrite: physical and chemical textures. Miner. Deposita 34, 82–101.
Cugerone, A., Cenki-Tok, B., Oliot, E., Muñoz, M., Barou, F., Motto-Ros, V., Le Goff, E., 2020. Redistribution of germanium during dynamic recrystallization of sphalerite. Geology. https://doi.org/10.1130/G46791.1.
Deditius, A.P., Utsunomiya, S., Renock, D., Ewing, R.C., Ramana, C.V., Becker, U., Kesler, S.E., 2008. A proposed new type of arsenian pyrite: composition, nanostructure and geological significance. Geochim. Cosmochim. Acta 72, 2919–2933.
Deditius, A.P., Reich, M., Kesler, S.E., Utsunomiya, S., Chryssoulis, S.L., Walshe, J., Ewing, R.C., 2014. The coupled geochemistry of Au and As in pyrite from hydrothermal ore deposits. Geochim. Cosmochim. Acta 140, 644–670.
Deditius, A.P., Reich, M., 2016. Constraints on the solid solubility of Hg, Tl, and Cd in arsenian pyrite. Am. Mineral. 101, 1451–1459.
Deditius, A.P., Utsunomiya, S., Reich, M., Kesler, S.E., Ewing, R.C., Hough, R., Walshe, J., 2011. Trace metal nanoparticles in pyrite. Ore Geol. Rev. 42, 32–46.
Fougerouse, D., Cugerone, A., Reddy, S.M., Luo, K., Motto-Ros, V., 2023. Nanoscale distribution of Ge in Cu–rich sphalerite. Geochim. Cosmochim. Acta 346, 223–230.
Frenzel, M., Hirsch, T., Gutzmer, J., 2016. Gallium, germanium, indium, and other trace and minor elements in sphalerite as a function of deposit type-a meta-analysis. Ore Geol. Rev. 76, 52–78.
Fu, J.N., Pirajno, F., Yang, F., Shivute, E., Sun, Y.Z., Ai, N., Qiu, K.F., 2021. Integration of zircon and apatite U-Pb geochronology and geochemical mapping of the Wude basalts (Emeishan large igneous province): a tool for abetter understanding of the tectonothermal and geodynamic evolution of the Emeishan LIP. Geosci. Front. 12, 573–585.
Gadd, M.G., Layton-Matthews, D., Peter, J.M., Paradis, S.J., 2016. The world–class Howard's Pass SEDEX Zn–Pb district, Selwyn Basin, Yukon. Part I: trace element compositions of pyrite record input of hydrothermal, diagenetic, and metamorphic fluids to mineralization. Miner. Deposita 51, 319–342.
Genna, D., Gaboury, D., 2015. Deciphering the hydrothermal evolution of a VMS system by LA–ICP–MS using trace elements in pyrite: an example from the Bracemac–McLeod deposits, Abitibi, Canada, and implications for exploration. Econ. Geol. 110, 2087–2108.
George, L., Cook, N.J., Ciobanu, C.L., Wade, B.P., 2015. Trace and minor elements in galena: a reconnaissance LA-ICP-MS study. Am. Mineral. 100 (2–3), 548–569.
Gregory, D.D., Larger, R.R., Halpin, J.A., Baturina, E.L., Lyons, T.W., Wu, S., Danyushevsky, L., Sack, P.J., Chappaz, A., Maslennikon, V.V., Bull, S.W., 2015. Trace element content of sedimentary pyrite in black shales. Econ. Geol. 110, 1389–1410.
Han, R.S., Zhang, Y., Wang, F., Wu, P., Qiu, W.L., Li, W.Y., 2019. Metallogenic mechanism and location prediction of concealed ore bodies of Germanium–rich silver–zinc–lead deposits in the polymetallic deposit concentrated district in Northeastern Yunnan, China. China Science Press, Beijing, pp. 1–510 in Chinese.
He, Y.F., Wu, T., Huang, Z.L., Ye, L., Deng, P., Xiang, Z.Z., 2020. Genesis of the Maoping carbonate–hosted Pb–Zn deposit, northeastern Yunnan Province, China: evidences from geology and C-O–S–Pb isotopes. Acta Geochimica 39, 782–796.
Hoefs, J., 2015. Stable Isotope Geochemistry, Seventh Edition. Springer, Cham, pp. 1–389.
Hou, L., Peng, H.J., Ding, J., Zhang, J.R., Zhu, S.B., Wu, S.Y., Wu, Y., Ouyang, H.G., 2015. Textures and in situ chemical and isotopic analyses of pyrite, Huijiabao Trend, Youjiang Basin, China: implications for paragenesis and source of sulfur. Econ. Geol. 111, 331–353.
Hu, R.Z., Fu, S.L., Huang, Y., Zhou, M.F., Fu, S.H., Zhao, C.H., Wang, Y.J., Bi, X.W., Xiao, J.F., 2017. The giant South China Mesozoic low–temperature metallogenic domain: reviews and a new geodynamic model. J. Asian Earth Sci. 137, 9–34.
Jiang, S.Y., Ma, Y., Liu, D.L., Li, W.T., 2023. Orogenic gold deposits: mineralization mechanism and research perspectives. J. Earth Sci. 34 (6), 1758–1761.
Keith, M., Häckel, F., Haase, K.M., Schwarz-Schampera, U., Klemd, R., 2016. Trace element systematics of pyrite from submarine hydrothermal vents. Ore Geol. Rev. 72, 728–745.
Koch, I., 2012. Analysis of multivariate and high-dimensional data theory and practice. Cambridge University Press, Cambridge, UK.
Koglin, N., Frimmel, H.E., Lawrie Minter, W.E., Brätz, H., 2010. Trace–element characteristics of different pyrite types in Mesoarchaean to Palaeoproterozoic placer deposits. Miner. Deposita 45, 259–280.
Kong, Z.G., Wu, Y., Liang, T., Zhang, F., Meng, X.Y., Lu, L., 2018. Sources of ore–forming material for Pb–Zn deposits in the Sichuan–Yunnan–Guizhou triangle area: Multiple constraints from C-H–O–S–Pb–Sr isotopic compositions. Geol. J. 53, 159–177.
Large, R.R., Maslennikov, V.V., Robert, F., Danyushevsky, L.V., Chang, Z.S., 2007. Multistage sedimentary and metamorphic origin of pyrite and gold in the giant Sukhoi Log deposit, Lena Gold Province, Russia. Econ. Geol. 102, 1233–1267.
Large, R.R., Danyushevsky, L.V., Hollit, C., Maslennikov, V., Meffre, S., Gilbert, S., Bull, S., Scott, R., Emsbo, P., Thomas, H., Foster, J., 2009. Gold and trace element zonation in pyrite using a laser imaging technique: implications for the timing of gold in orogenic and carlin–style sediment hosted deposits. Econ. Geol. 104, 635–668.
Large, R.R., Bull, S.W., Maslennikov, V.V., 2011. A carbonaceous sedimentary source–rock model for carlin–type and orogenic gold deposits. Econ. Geol. 106, 331–358.
Large, R.R., Halpin, J.A., Danyushevsky, L.V., Maslennikov, V.V., Bull, S.W., Long, J.A., Gregory, D.D., Lounejeva, E., Lyons, T.W., Sack, P.J., 2014. Trace element content of sedimentary pyrite as anew proxy for deep–time ocean–atmosphere evolution. Earth Planet. Sci. Lett. 389, 209–220.
Large, R.R., Mukherjee, I., Gregory, D., Steadman, J., Corkrey, R., Danyushevsky, L.V., 2019. Atmosphere oxygen cycling through the proterozoic and phanerozoic. Miner. Deposita 54, 485–506.
Leach, D.L., Bradley, D., Lewchuk, M.T., Symons, D.T., Marsily, G.D., Brannon, J., 2001. Mississippi Valley–type lead–zinc deposits through geological time: implications from recent age–dating research. Miner. Deposita 36, 11–740.
Leach, D.L., Sangster, D.F., Kelley, K.D., Large, R.R., Garven, G., Allen, C.R., Gutzmer, J., Walters, S.G., 2005. Sediment–hosted lead–zinc deposits: a global perspective. Econ. Geol. 100, 561–607.
Leach, D.L., Bradley, D.C., Huston, D., Pisarevsky, S.A., Taylor, R.D., Gardoll, S.J., 2010. Sediment–hosted lead–zinc deposits in Earth history. Econ. Geol. 105, 593–625.
Leach, D.L., Song, Y.L., 2019. Sediment–hosted zinc–lead and copper deposits in China. SEG Special Publications 22, 325–409.
Li, D.F., Chen, H.Y., Sun, X.M., Fu, Y., Liu, Q.F., Xia, X.P., Yang, Q., 2019a. Coupled trace element and SIMS sulfur isotope geochemistry of sedimentary pyrite: implications on pyrite growth of Caixiashan Pb–Zn deposit. Geosci. Front. 10, 2177–2188.
Li, N., Deng, J., Yang, L.Q., Goldfarb, R.J., Zhang, C., Marsh, E., Lei, S.B., Koenig, A., Lowers, H., 2014. Paragenesis and geochemistry of ore minerals in the epizonal gold deposits of the Yangshan gold belt, West Qinling, China. Miner. Deposita 49, 427–449.
Li, Z.L., Ye, L., Hu, Y.S., Wei, C., Huang, Z.L., Nian, H.L., Cai, J.J., Danyushevsky, L., 2019c. Trace (dispersed) elements in pyrite from the Fule Pb–Zn deposit, Yunnan Province, China, and its genetic information: a LA–ICP–MS study. Acta Petrol. Sin. 35, 3370–3384 in Chinese with English abstract.
Li, H.B., Zhang, Z.C., Santosh, M., Li, Y.S., Han, L., Zhu, J., Pan, R.H., 2019b. Geochronological, geochemical and Sr–Nd isotopic fingerprinting of Neoproterozoic mafic dykes in the western margin of the Yangtze Block, SW China: implications for Rodinia supercontinent breakup. Precambr. Res. 331, 105371.
Liu, Y.S., Hu, Z.C., Gao, S., Günther, D., Xu, J., Gao, C.G., Chen, H.L., 2008. In situ analysis of major and trace elements of anhydrous minerals by LA–ICP–MS without applying an internal standard. Chem. Geol. 257, 34–43.
Luo, K., Cugerone, A., Zhou, M.F., Zhou, J.X., Sun, G.T., Xu, J., He, K.J., Lu, M.D., 2022. Germanium enrichment in sphalerite with acicular and euhedral textures: an example from the Zhulingou carbonate-hosted Zn(-Ge) deposit, South China. Mineralium Deposita 57, 1343–1365.
Makoundi, C., Zaw, K., Large, R.R., Meffre, S., Lai, C.K., Hoe, T.G., 2014. Geology, geochemistry and metallogenesis of the Selinsing gold deposit, central Malaysia. Gondwana Res. 26, 241–261.
Miao, Y., Li, w.c., Zhou, J.X., Luo, K., Zhou, Y., Chen, S.M., Fan, Z.Y., Pan, J.R., 2023. Geology, geochemistry and genesis of the giant Maoping carbonate-hosted Pb-Zn-(Ag-Ge) deposit in northeastern Yunnan Province, SW China. Ore Geology Reviews, 161, 105648.
Mukherjee, I., Large, R.R., 2020. Co–evolution of trace elements and life in Precambrian oceans: The pyrite edition. Geology, 48, 1018–1022.
Niu, P.P., Jiang, S.Y., Xiong, S.F., Hu, Q.S., Xu, T.L., 2019. Geological characteristics, fluid inclusions and H-O–C–S isotopes of the Zaopa Ag–Mo prospect in the Suizao area, Hubei Province: implications for ore genesis. Ore Geol. Rev. 111, 103012.
Niu, P.P., Jiang, S.Y., Munoz, M., 2023. Two-stage enrichment of germanium in the giant Maoping MVT Pb-Zn deposit, southwestern China: constraints from in situ analysis of multicolor sphalerites. Ore Geol. Rev. 157, 105421.
Niu, P.P., Munoz, M., Mathon, O., Xiong, S.F., Jiang, S.Y., 2024. Mechanism of germanium enrichment in the world-class Huize MVT Pb–Zn deposit, southwestern China. Miner. Deposita. https://doi.org/10.1007/s00126-023-01242-3.
Ohmoto, H., Rye, R.O., 1979. Isotopes of sulfur and carbon. In: Geochemistry of Hydrothermal Ore Deposits. Barnes HL (ed) J Wiley and Sons, 509-567.
Perfetti, E., Pokrovski, G.S., Ballerat-Busserolles, K., Majer, V., Gibert, F., 2008. Densities and heat capacities of aqueous arsenious and arsenic acid solutions to 350°C and 300 bar, and revised thermodynamic properties of, and iron sulfarsenide minerals. Geochim. Cosmochim. Acta 72 (3), 713–731.

Pfaff, K., Koenig, A., Wenzel, T., Ridley, I., Hildebrandt, L.H., Leach, D.L., Markl, G., 2011. Trace and minor element variations and sulfur isotopes in crystalline and colloform ZnS: Incorporation mechanisms and implications for their genesis. Chem. Geol. 286, 118–134.
Pokrovski, G.S., Kara, S., Roux, J., 2002. Stability and solubility of arsenopyrite, FeAsS, in crustal fluids. Geochim. Cosmochim. Acta 66, 2361–2378.
Reddy, S.M., Hough, R.M., 2013. Microstructural evolution and trace element mobility in Witwatersrand pyrite. Contribution to Mineralogy and Petrology 166, 1269–1284.
Reich, M., Becker, U., 2006. First–principles calculations of the thermodynamic mixing properties of arsenic incorporation into pyrite and marcasite. Chem. Geol. 225, 278–290.
Reich, M., Simon, A., Deditius, A., Barra, F., Chrysoullis, S., Lagas, G., Tardani, D., Knipping, J., Bilenker, L., Sánchez, P., Roberts, M., Minizaga, R., 2016. Trace element signature of pyrite from the los colorados iron oxide–apatite (IOA) Deposit, Chile: a missing link between Andean Ioa and iron oxide copper–gold systems? Econ. Geol. 111, 743–761.
Ren, S.L., Li, Y.H., Zeng, P.S., Qiu, W.L., Fan, C.F., Hu, G.Y., 2018. Effect of sulfate evaporate salt layer in mineralization of the Huize and Maoping lead–zinc deposits in Yunnan: evidence from sulfur isotope. Acta Geologica Sinica. 92, 1041–1055 (in Chinese with English abstract).
Schrader, D.L., Davidson, J., McCoy, T.J., Zega, T.J., Russell, S.R., Domanik, K.J., King, A.J., 2021. The Fe/S ratio of pyrrhotite group sulfides in chondrites: an indicator of oxidation and implications for return samples from asteroids Ryugu and Bennu. Geochim. Cosmochim. Acta 303, 66–91.
Seal, R.R., 2006. Sulfur isotope geochemistry of sulfide minerals. Rev. Mineral. Geochem. 61, 633–677.
Shelton, K.L., Gregg, J.M., Johnson, A.W., 2008. Replacement dolomites and ore sulfides as recorders of multiple fluids and fluid sources in the southeast Missouri Mississippi Valley–type district: Halogen– $^{87}Sr/^{86}Sr$–$\delta^{18}O$–$\delta^{34}S$ systematics in the Bonneterre dolomite. Econ. Geol. 104, 733–748.
Song, X.Y., Chen, L.M., Yu, S.Y., Tao, Y., She, Y.W., Luan, Y., Zhang, X.Q., He, H.L., 2018. Geological features and genesis of the V-Ti magenetite deposits in the Emeishan large igneous province, southwest China. Bull. Mineral. Petrol. Geochem. 37, 1003–1018.
Song, K.R., Tang, L., Zhang, S.T., Santosh, M., Spencer, C.J., Zhao, Y., Li, H.X., Wang, L., Zhang, A.L., Sun, Y.Q., 2019. Genesis of the Bianjiadayuan Pb-Zn polymetallic deposit, Inner Mongolia, China: Constraints from in–situ sulfur isotope and trace element geochemistry of pyrite. Geosci. Front. 10, 1863–1877.
Steadman, J.A., Large, R.R., Olin, P.H., Danyushevsky, L.V., Meffre, S., Huston, D., Fabris, A.M., Lisitsin, V., Wells, T., 2021. Pyrite trace element behavior in magmatic–hydrothermal environments: an LA–ICPMS imaging study. Ore Geol. Rev. 128, 103878.
Tan, S.C., Zhou, J.X., Luo, K., Xiang, Z.Z., He, X.H., Zhang, Y.H., 2019. The sources of ore–forming elements of the Maoping large–scale Pb–Zn deposit, Yunnan Province: constrains from in–situ S and Pb isotopes. Acta Petrol. Sin. 35, 3461–3476 in Chinese with English abstract.
Tang, Q.Y., Li, C.S., Ripley, E.M., Bao, J., Su, T.B., Xu, T.B., 2021. Sr–Nd–Hf–O isotope constraints on crustal contamination and mantle source variation of three Fe–Ti–V oxide ore deposits in the Emeishan large igneous province. Geochim. Cosmochim. Acta 292, 364–381.
Thomas, H.V., Large, R.R., Bull, S.W., Maslennikov, V., Berry, R.F., Fraser, R., Froud, S., Moye, R., 2011. Pyrite and pyrrhotite textures and composition in sediments, laminated quartz veins, and reefs at Bendigo gold mine, Australia: insights for ore genesis. Econ. Geol. 106, 1–31.
Wang, C.M., Deng, J.M., Carranza, E.J., Lai, X.R., 2014. Nature, diversity and temporal–spatial distributions of sediment–hosted Pb–Zn deposits in China. Ore Geol. Rev. 56, 327–351.
Wang, L., Han, R.S., Zhang, Y., Li, X.D., 2023. Mixing in two types of fluids responsible for some carbonate-hosted Pb-Zn deposits, SW China: insights from the maoping deposit. Minerals 13 (5), 600.
Wang, C.M., Yang, L.F., Bagas, L., Evans, N.J., Chen, J.Y., Du, B., 2018. Mineralization processes at the giant Jinding Zn–Pb deposit, Lanping Basin, Sanjiang Tethys Orogen: evidence from in situ trace element analysis of pyrite and marcasite. Geol. J. 53, 1279–1294.
Wilkinson, J.J., Eyre, S.L., 2005. Ore–forming processes in Irish–type carbonate–hosted Zn–Pb deposits: evidence from mineralogy, chemistry, and isotopic composition of sulfides at the Lisheen mine. Econ. Geol. 100, 63–86.
Worden, R.H., Smalley, P.C., Oxtoby, N.H., 1995. Gas souring by the thermo chemical sulfate reduction at 140°C. AAPG Bull. 79, 854–863.
Wu, J.B., Han, R.S., Zhang, Y., Sun, B.T., Li, W.Y., Li, D.Q., Cao, Y.R., Cen, C., 2024. The fault–fold structure ore control mechanism of hydrothermal deposits——a case study of the Maoping super-large rich-Ge lead–zinc deposit in northeastern Yunnan China. Ore Geol. Rev. 168, 106039.
Wu, T., Huang, Z.L., Xiang, Z.Z., Ye, L., Sui, Z.H., Hu, Y.S., Yan, Z.F., 2020. In situ trace element study of pyrites from the Danaopo super–large Pb–Zn deposit in the western Hunan, China. Acta Mineralogica Sinica 40, 430–440 in Chinese with English abstract.
Wu, T., Huang, Z.L., He, Y.F., Yang, M., Fan, H.F., Chen, W., Ye, L., Hu, Y.S., Xiang, Z.Z., Lai, C.K., 2021. Metal source and ore–forming process of the Maoping carbonate–hosted Pb–Zn deposit in Yunnan, SW China: evidence from deposit geology and sphalerite Pb–Zn–Cd isotopes. Ore Geol. Rev. 135, 104214.
Wu, Y., Zhang, C.Q., Mao, J.W., Ouyang, H.G., Sun, J., 2013. The genetic relationship between hydrocarbon systems and Mississippi Valley–type Zn–Pb deposits along the SW margin of Sichuan Basin, China. Int. Geol. Rev. 55, 941–957.
Xiang, Z.Z., Zhou, J.X., Luo, K., 2020. New insights into the multi–layer metallogenesis of carbonated–hosted epigenetic Pb–Zn deposits: a case study of the Maoping Pb–Zn deposit South China. Ore Geol. Rev. 122, 103538.
Xiao, X., Zhou, T.F., White, N.C., Zhang, L.J., Fan, Y., Wang, F.Y., Chen, X.F., 2018. The formation and trace elements of garnet in the skarn zone from the Xinqiao Cu–S–Fe–Au deposit, Tongling ore district, Anhui Province, Eastern China. Lithos 302–303, 467–479.
Xing, Y., Brugger, J., Tomkins, A., Shvarov, Y., 2019. Arsenic evolution as a tool for understanding formation of pyritic gold ores. Geology 47, 335–338.
Xu, C., Zhong, H., Hu, R.Z., Wen, H.J., Zhu, C.W., Bai, Z.J., Fan, H.F., Li, F.F., Zhou, T., 2020. Sources and ore–forming fluid pathways of carbonate–hosted Pb–Zn deposits in Southwest China: implications of Pb–Zn–S–Cd isotopic compositions. Miner. Deposita 55, 491–513.
Yang, Q., Liu, W.H., Zhang, J., Wang, J., Zhang, X.J., 2019. Formation of Pb–Zn deposits in the Sichuan–Yunnan–Guizhou triangle linked to the Youjiang foreland basin: evidence from Rb–Sr age and in situ sulfur isotope analysis of the Maoping Pb–Zn deposit in northeastern Yunnan Province, southeast China. Ore Geol. Rev. 107, 780–800.
Yuan, B., Zhang, C.Q., Yu, H.J., Yang, Y.M., Zhao, Y.X., Zhu, C.C., Ding, Q.F., Zhou, Y.B., Yang, J.C., Xu, Y., 2018. Element enrichment characteristics: Insights from element geochemistry of sphalerite in Daliangzi Pb-Zn deposit, Sichuan, Southwest China. J. Geochem. Explor. 186, 187–201.
Zhang, R.X., Yang, S.Y., 2016. A mathematical model for determining carbon coating thickness and its application in electron probe microanalysis. Microscopy and Microanalysis, 22, 1374–1380.
Zhang, S.B., Zheng, Y.F., 2013. Formation and evolution of Precambrian continental lithosphere in South China. Gondwana Research, 23, 1241–1260.
Zhang, Q.Q., Gao, X.Y., Zhang, S.B., Zheng, Y.F., 2020. Paleoproterozoic tectonic evolution of the northern Yangtze craton from oceanic subduction through continental collision to continental rifting: geochronological and geochemical records of metabasites from the Tongbai orogen in central China. Precambr. Res. 23, 1189–1206.
Zhang, W.D., Li, B., Lu, A.H., Zhao, K.D., Elatikpo, S.M., Chen, X.D., Zhu, L.Z., Yu, M., 2022. In–situ pyrite trace element and sulfur isotope characteristics and metallogenic implications of the Qixiashan Pb–Zn–Ag polymetallic deposit. Eastern China. Ore Geology Reviews 144, 104849.
Zhang, C.Q., Rui, Z.Y., Chen, Y.C., Wang, D.H., Chen, Z.H., Lou, D.B., 2013. The main successive strategic bases of resources for Pb–Zn deposits in China. Geol. China 40, 248–272 in Chinese with English abstract.
Zhang, C.Q., Wu, Y., Hou, L., Mao, J.W., 2015. Geodynamic setting of mineralization of Mississippi Valley–type deposits in world–class Sichuan–Yunnan–Guizhou Zn–Pb triangle, Southwest China: Implications from age–dating studies in the past decade and the Sm–Nd age of Jinshachang deposit. J. Asian Earth Sci. 103, 103–114.
Zhao, J.H., Li, Q.W., Liu, H., Wang, W., 2018. Neoproterozoic magmatism in the western and northern margins of the Yangtze Block (South China) controlled by slab subduction and subduction–transform–edge–propagator. Earth Sci. Rev. 187, 1–18.
Zhao, W.C., Zhu, X.Y., Jiang, B.B., Zhao, D.S., 2023. Genesis of the carbonate-hosted zinc–lead deposits in the southwestern Yangtze Craton, SW China: Insights from the Maoping deposit. J. Geochem. Explor. 250, 107234.
Zheng, Y.F., Xiao, W.J., Zhao, G.C., 2013. Introduction to tectonics of China. Gondw. Res. 23, 1189–1206.
Zhou, J.X., Huang, Z.L., Zhou, M.F., et al., 2013. Constraints of C-O–S–Pb isotope compositions and Rb–Sr isotopic age on the origin of the Tianqiao carbonate–hosted Pb–Zn deposit, SW China. Ore Geol. Rev. 53, 77–92.
Zhou, J.X., Huang, Z.L., Zhou, M.F., Zhu, X.K., Muchez, P., 2014. Zinc, sulfur and lead isotopic variations in carbonate–hosted Pb–Zn sulfide deposits, southwest China. Ore Geol. Rev. 58, 41–54.
Zhu, Z.Y., Jiang, S.Y., Ciobanu, C.L., Yang, T., Cook, N.J., 2017. Sulfur isotope fractionation in pyrite during laser ablation: implications for laser ablation multiple collector inductively coupled plasma mass spectrometry mapping. Chem. Geol. 450, 223–234.
Zhu, C.W., Wang, J., Zhang, J.W., Chen, X.C., Fan, H.F., Zhang, Y.X., Yang, T., Wen, H.J., 2020. Isotope geochemistry of Zn, Pb and S in the Ediacaran strata hosted Zn-Pb deposits in Southwest China. Ore Geol. Rev. 117, 103274.